



Title	Anisotropic defect distribution in He <sup>+</sup> -irradiated 4H-SiC: Effect of stress on defect distribution
Author(s)	Yang, Subing; Nakagawa, Yuki; Kondo, Minako; Shibayama, Tamaki
Citation	Acta materialia, 211, 116845 <a href="https://doi.org/10.1016/j.actamat.2021.116845">https://doi.org/10.1016/j.actamat.2021.116845</a>
Issue Date	2021-06-01
Doc URL	<a href="http://hdl.handle.net/2115/88735">http://hdl.handle.net/2115/88735</a>
Rights	© <2021>. This manuscript version is made available under the CC-BY-NC-ND 4.0 license <a href="http://creativecommons.org/licenses/by-nc-nd/4.0/">http://creativecommons.org/licenses/by-nc-nd/4.0/</a>
Rights(URL)	<a href="http://creativecommons.org/licenses/by-nc-nd/4.0/">http://creativecommons.org/licenses/by-nc-nd/4.0/</a>
Type	article (author version)
File Information	Manuscript_revised-unmarked.pdf



[Instructions for use](#)

1 **Anisotropic defect distribution in He<sup>+</sup>-irradiated 4H-SiC:**  
2 **effect of stress on defect distribution**

3 Subing Yang, Yuki Nakagawa, Minako Kondo, Tamaki Shibayama\*

4 Faculty of Engineering, Hokkaido University, Sapporo, Hokkaido 060-8628, Japan

5 \* Corresponding author.

6 E-mail address: shiba@qe.eng.hokudai.ac.jp

7

8

9

10

11

12

13

14

15

16

17

18

19

20

21

22 **Abstract**

23 Irradiation-induced anisotropic swelling in hexagonal  $\alpha$ -SiC is known to  
24 degrade the mechanical properties of SiC; however, the associated physical  
25 mechanism and microstructural process remain insufficiently understood.  
26 In this study, an anisotropic swelling condition where the surface normal  
27 direction was allowed to freely expand with constraint in the lateral  
28 direction was introduced in 4H-SiC using selected-area He<sup>+</sup> irradiation, and  
29 the internal defect distribution was investigated using transmission electron  
30 microscopy (TEM) and advanced scanning TEM. The defect distribution  
31 was compared to that in non-selected-area He<sup>+</sup>-irradiated 4H-SiC and  
32 electron-irradiated TEM-foil 4H-SiC. An anisotropic defect distribution  
33 was observed in the selected-area He<sup>+</sup>-ion-irradiated 4H-SiC, with  
34 interstitial defects preferentially redistributed in the surface normal  
35 direction ([0004]) and negative volume defects (such as vacancies and/or  
36 carbon antisite defects) dominantly located in the lateral directions ([11 $\bar{2}$ 0]  
37 and [10 $\bar{1}$ 0]). This anisotropy of the defect distribution was substantially  
38 lower in the non-selected-area He<sup>+</sup>-irradiated and electron-irradiated  
39 samples. The stress condition in the three samples was also measured and  
40 analyzed. In the selected-area He<sup>+</sup>-irradiated 4H-SiC, compressive stress  
41 was introduced in the lateral directions (([10 $\bar{1}$ 0] and [11 $\bar{2}$ 0])), with little  
42 stress introduced in the surface normal direction ([0004]); this stress  
43 condition was introduced at the beginning of ion irradiation. The  
44 compressive stress likely inhibits the formation of interstitial defects in the  
45 lateral directions, enhancing the anisotropy of the defect distribution in

46 SiC.

47 **Keywords:** Silicon carbide; Irradiation effect; Swelling; Defects; TEM.

## 48 **1. Introduction**

49 Because of its excellent mechanical, structural, and electronic properties,  
50 silicon carbide (SiC) has been proposed as an excellent candidate for  
51 various nuclear, aerospace, and electronic applications [1-4]. SiC is  
52 exposed to various types of irradiation during the fabrication of electronic  
53 devices (such as ion implantation for doping carriers) or when applied in  
54 nuclear or aerospace environments (neutron or other high-energy particle  
55 irradiations) [5-6]. This irradiation inevitably introduces damage, which  
56 greatly affects the mechanical and electronic properties. Particular interest  
57 has been focused on irradiation-induced dimension instability, including  
58 swelling [7] and creeping [8], which is a key issue for long-term structural  
59 performance in nuclear reactors. In order to resolve these issues, one of the  
60 key challenges is to simulate the various damages introduced by neutron  
61 irradiation. Neutron irradiation could induce a displacement cascade of  
62 lattice atoms, and various defects would form with diffusion and  
63 combination of the displaced lattice atoms. However, currently neutron  
64 irradiation experiments are hampered by long time, expensive cost and high  
65 radioactivity [9]. High energy electron irradiation could also induce  
66 displacement of lattice atoms that it can be used to simulate the irradiation  
67 damage. Although it has a higher irradiation flux and damage rates, it  
68 cannot cause the displacement cascade. Also, its penetration depth is thin,

69 and it is usually performed on the foil sample. To some extent, energetic  
70 ion irradiation is a promising simulation method, which not only could  
71 induce the displacement cascade of lattice atoms, but also has the  
72 advantages of high damage rates, minimal residual radio activity and low  
73 cost [9]. The application of modern materials modeling methods has also  
74 made great progress to study radiation effects on SiC. Y. Katoh et al. [10]  
75 has reported the recent advances and outstanding challenges in modeling of  
76 radiation induced defects and their interactions with microstructure,  
77 transport of fission products through SiC, and thermomechanical properties  
78 of SiC, which shows that such modeling can be powerful for the design of  
79 SiC-based materials for the harsh environments encountered in fission and  
80 fusion applications. Using first-principles density functional theory  
81 calculations, N. Daghbouj et al. [11] advanced the understanding of the  
82 mechanism of the bubble-to-platelet transition in the He<sup>+</sup>-irradiated 6H-SiC.  
83 Due to the small size of defect clusters (such as < 1 nm) that they are  
84 difficult to measure in traditional TEM, hence, how to measure and  
85 quantify their distribution is an outstanding challenge. Recently, C. Liu, I.  
86 Szlufarska and their coworker [7] developed a cluster dynamics model that  
87 can describe the evolution of irradiation-induced defects, and this mode  
88 closes the gap between simulation and experimental results in terms of the  
89 cluster size distribution.

90 In the previously reported studies, sufficient effort has been dedicated to  
91 investigating the irradiation-induced swelling in SiC. S. Leclerc et al. has  
92 reported swelling of He<sup>+</sup>-irradiated 4H-SiC at different fluences, different

93 irradiation temperature [12] and different annealing temperature [13]. They  
94 have well characterized swelling, disorder and defects evolution in  
95 irradiated SiC, moreover, the contribution of different types of defects or  
96 damage to swelling was also classified. The disordering behavior, up to  
97 amorphization, of both irradiated 6H-SiC and 3C-SiC polytypes was  
98 successfully characterized and modelled by A. Debelle et al. [14], and the  
99 simulation results were consistent with the experimental results. In these  
100 reported results, most investigations were focused on the  
101 irradiation-induced isotropic swelling. However, apart from conventional  
102 isotropic swelling, irradiation may induce anisotropic swelling in  
103 hexagonal-crystal  $\alpha$ -SiC [15], which has also been observed in many other  
104 hexagonal-crystal ceramic materials including aluminum nitride [16],  
105 silicon nitride [17], titanium aluminum carbide [18], and titanium silicon  
106 carbide [19]. Besides, it has also been reported that the thermal expansion  
107 coefficients of  $\alpha_{11}$  is  $3.21 \times 10^{-6}$ ,  $5.6 \times 10^{-6}$  and  $12.9 \times 10^{-6}$  ( $1/^\circ\text{C}$ ) for 4H-SiC  
108 [20], AlN [21], and Cr<sub>2</sub>GeC [22], but  $\alpha_{33}$  is  $3.09 \times 10^{-6}$ ,  $6.9 \times 10^{-6}$ ,  $17.6 \times 10^{-6}$   
109 ( $1/^\circ\text{C}$ ), respectively. Up to now, the irradiation-induced anisotropic  
110 swelling in  $\alpha$ -SiC was still insufficient. Compared with isotropic swelling,  
111 anisotropic swelling is more deleterious in terms of the resulting  
112 degradation of mechanical properties. The swelling itself is not considered  
113 a key limitation for the application of SiC in nuclear reactors; however, the  
114 significant internal stress induced by differential swelling can lead to  
115 degradation of the component structures [18,23,24]. Moreover, fractures or  
116 microcracks have also been reported to preferentially occur at the grain

117 boundaries in materials with such anisotropic swelling [18,19]. It appears  
118 reasonable that  $\alpha$ -SiC and other ceramics with a hexagonal crystal structure  
119 may display differing irradiation-induced expansion in different directions,  
120 leading to loss of the original crystal integrity and degradation of the  
121 mechanical properties. However,  $\alpha$ -SiC can also exhibit isotropic swelling.  
122 For example, L.L. Snead et al. reported an essentially equivalent dilation of  
123 the  $\langle a \rangle$  and  $\langle c \rangle$  axes for neutron-irradiated  $\alpha$ -6H-SiC near 60 °C [25]. In  
124 addition, Y. Lin and coworkers also observed anisotropic crystal swelling in  
125  $\text{Si}^{2+}$ -irradiated cubic- $\beta$ -3C SiC at 1000 °C [26]. Furthermore, the variation  
126 of swelling behavior for both  $\alpha$ - and  $\beta$ -SiC resulting from different  
127 irradiation conditions (different irradiation particles, doses, and  
128 temperatures) [25,27,28] complicates the understanding of anisotropic  
129 swelling in SiC. To date, the underlying mechanism of this anisotropic  
130 swelling remains far from well understood in terms of the physical  
131 mechanism and microstructural process.

132 According to the correlation of defects with swelling, with volumetric  
133 swelling dominated by various defects, especially point defects or tiny  
134 defect clusters at room temperature [7,29], it is reasonable to consider that  
135 anisotropic swelling should be correlated to the defect distribution for  
136 different crystal orientations. Various attempts have been made to explore  
137 the defect distribution and disorder accumulation in irradiated  $\alpha$ -SiC. Jiang  
138 et al. observed anisotropic lattice expansion in  $\text{H}^+$ -implanted  $\alpha$ -6H-SiC at  
139 extremely low doses below 340 K. In that study, the anisotropic swelling  
140 was mainly attributed to irradiation-induced vacancies in the basal plane

141 based on a theoretical analysis [27]. However, the defect distribution in the  
142 samples was not provided. Zhang et al. [30] observed an anisotropy of  
143 disorder accumulation in  $\text{Au}^+$ -irradiated  $\alpha$ -4H-SiC at 165 K using  
144 Rutherford backscattering spectroscopy, which was well explained by the  
145 stable defect configuration with most interstitial configurations parallel to  
146 the [0001] direction according to the molecular dynamic simulation.  
147 However, it is not clear that this anisotropic disorder accumulation occurs  
148 for anisotropic or isotropic swelling in SiC. Therefore, to obtain insight into  
149 the anisotropic swelling mechanism, a fundamental understanding of the  
150 detailed defect distribution for different orientations or planes in SiC with  
151 anisotropic swelling is needed. However, the defect distribution in  $\alpha$ -SiC  
152 with anisotropic swelling has rarely been reported because of the relatively  
153 small size of the defects, which are difficult to observe using conventional  
154 transmission electron microscopy (TEM), especially at relatively low  
155 irradiation temperature [7].

156 Kondo et al. [31] explored the stable surface class in 6H-SiC by  
157 analyzing nano-void shapes using TEM, which suggests that the  
158 observation of some second-type defects formed by the accumulation of  
159 point defects might provide insight into the defect distribution in irradiated  
160  $\alpha$ -SiC. In addition, in our previous study, anisotropic swelling or strain was  
161 introduced in 4H-SiC using selected-area ion irradiation, as demonstrated  
162 by atomic force microscopy and electron back scattering diffraction  
163 (EBSD) [32]. Hence, this approach might be useful to explore the  
164 phenomenon and underlying mechanism of anisotropic swelling in SiC. In



165 the current study, anisotropic swelling was introduced in 4H-SiC using  
166 selected-area ion irradiation, and the defect distribution in different  
167 directions was explored using various TEM techniques. An anisotropic  
168 defect distribution was observed in the irradiated 4H-SiC. In addition, the  
169 potential mechanism for this defect distribution is discussed.

## 170 **2. Experimental procedures**

171 Single-crystalline n-type 4H-SiC (0001) substrates (Xiamen Powerway  
172 Advanced Material Co., Ltd., Xiamen, China) with dimensions of  $10 \times 10$   
173  $\times 0.33 \text{ mm}^3$  were irradiated with 100-keV  $\text{He}^+$  at room temperature to  
174 fluences of  $1 \times 10^{15}$  and  $5 \times 10^{16} \text{ cm}^{-2}$ . During irradiation, the irradiation flux  
175 was kept at a level of  $6.2 \times 10^{12} \text{ He} \cdot \text{cm}^{-2} \cdot \text{s}^{-1}$ , and the beam raster scanning  
176 was performed to reach a homogeneous irradiation condition in the  
177 irradiated area.

178 For comparison, both selected-area irradiation and non-selected-area  
179 irradiation were performed. During selected-area irradiation, part of the  
180 sample was covered by a mask with a hole 8 mm in diameter to clearly  
181 distinguish between the irradiated and unirradiated areas. More details of  
182 the selected-area ion irradiation procedure are provided in Ref. [32]. The  
183 non-selected-area irradiation, i.e., without using the mask, was also  
184 prepared at room temperature with a fluence of  $5 \times 10^{16} \text{ cm}^{-2}$ . The damage  
185 and injected helium profile for  $\text{He}^+$  into SiC were calculated using SRIM  
186 2013 in full-cascade mode. The sample density and threshold displacement  
187 energy for the C and Si sub-lattices used in the calculation were 3.21  
188  $\text{g} \cdot \text{cm}^{-3}$  and 21 and 35 eV [33], respectively. The total penetration depth

189 predicted by simulation was approximately 600 nm, and the highest  
190 damage was predicted to occur at approximately 450 nm with a dose of  
191 about 4.2 dpa (displacement per atom, dpa) for the fluence of  $5 \times 10^{16} \text{ cm}^{-2}$   
192 [34]. In addition, a peak helium concentration of about 2.95% is observed  
193 at about 470 nm in depth.

194 After irradiation, cross-sectional thin foils for TEM were prepared from  
195 irradiated areas using gallium ions in a focused-ion-beam system (JEOL,  
196 JEM-90320FIB). The ion accelerating voltage was 30 kV, and the samples  
197 were thinned to a final thickness of about 100 nm. To minimize the damage  
198 introduced into the TEM samples by gallium ions during FIB, these TEM  
199 samples were then polished by lower energy Ar ions using GentleMill  
200 (TECHNOORG-IINDA ltd. Co., Gentle Mill IV8 HI). Both sides of TEM  
201 samples were polished with a 1.5 kV beam at  $8^\circ$  incident angle for 40 mins,  
202 then 0.5 kV at  $15^\circ$  for 30 mins. The microstructural features of the  
203 irradiated 4H-SiC were observed using TEM (JEOL, JEM-2000FX) at an  
204 operation voltage of 200 kV. The average size and number density of  
205 defects were counted and calculated from weak-beam dark-field TEM  
206 images, with 3–5 images used for each calculation. The TEM images used  
207 for damage counting are all taken at the same magnification, then adjusted  
208 to the same background contrast and brightness using Gatan  
209 DigitalMicrograph. The BSDs were then marked by Adobe Photoshop  
210 based on the contrast difference from the background, which could be  
211 automatically counted using the software of MAC-View Version.4  
212 (Mountech Co., Ltd.). The average size of a BSD was recorded by the

213 Heywood diameter. The thicknesses of the observation regions were  
214 measured using electron energy loss spectroscopy (EELS) with a  
215 Cs-corrected scanning transmission electron microscope (FEI, Titan G2  
216 60-300). High-resolution TEM (HR-TEM) analysis, high-angle annular  
217 dark field (HAADF) and annular bright field (ABF) scanning transmission  
218 electron microscopy (STEM), and core-loss EELS studies were also  
219 performed using the Cs-corrected STEM. The operation voltage was 300  
220 kV. HAADF- and ABF-STEM images were simultaneously obtained with a  
221 17.8-mrad semi-convergence angle and 50–200 and 10.36–24.48 mrad  
222 collection angles for the HAADF and ABF mode, respectively.

223 Together with the strain, the elastic stress in the irradiated area was also  
224 determined using EBSD and Crosscourt3 software with the elasticity  
225 coefficients of 4H-SiC. A field-emission scanning electron microscope  
226 (JEOL JSM–7001FA) equipped with an EBSD detector was used to obtain  
227 EBSD patterns, operating at an acceleration voltage of 20 kV, a sample tilt  
228 of 70°, and a scan size and scan step of 20×20 μm<sup>2</sup> and 0.1 μm, respectively.  
229 The elasticity coefficients provided by the Crosscourt3 software, C11=501  
230 GPa, C12=111 GPa, C13=52 GPa, C22=501 GPa, C33=553 GPa, and  
231 C44=163 GPa, were consistent with previously reported results [35]. The  
232 stress was determined by analyzing the EBSD patterns using the  
233 CrossCourt3 software. Details of this strain/stress measurement method  
234 using EBSD and the strain results have been published elsewhere (Ref.  
235 [32]).

236 Electron irradiation of thin-foil 4H-SiC samples using a multi-beam

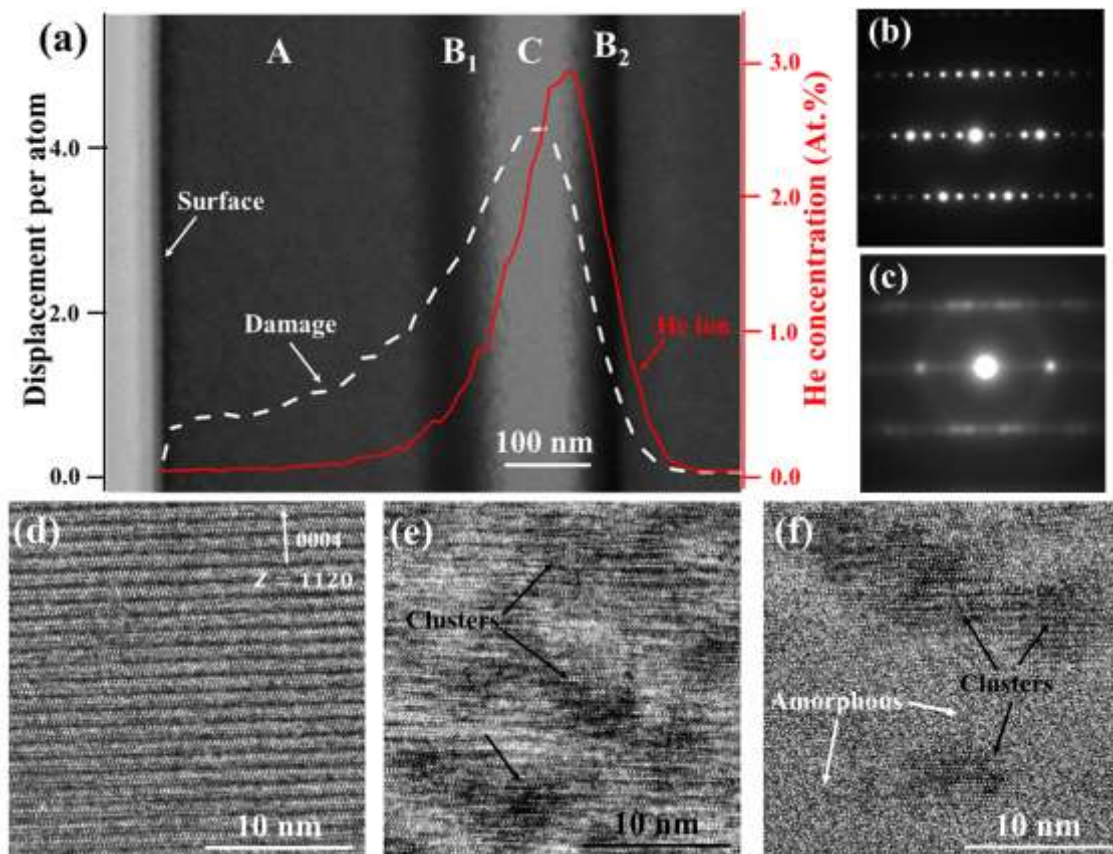
237 ultra-high voltage electron microscope (multi-beam HVEM, JEOL,  
238 JEM-ARM1300) was also performed. The TEM samples for electron  
239 irradiation were prepared from unirradiated areas of the selected-area  
240 He<sup>+</sup>-irradiated 4H-SiC samples using FIB; before electron irradiation, the  
241 TEM samples were annealed at 600 °C for 30 min in the multi-beam  
242 HVEM to remove any potential internal stress. The electron irradiation was  
243 performed at room temperature at an accelerating voltage of 1.25 MV with  
244 an irradiation area diameter of approximately 2 μm. The electron flux was  
245 approximately  $1.2 \times 10^{24} \text{ e} \cdot \text{m}^{-2} \cdot \text{s}^{-1}$ , and the total irradiation time was 1 h.  
246 During irradiation, the electron beam was controlled to be parallel to the  
247  $[11\bar{2}0]$  orientation. After electron irradiation, the defect distribution in  
248 electron-irradiated thin-foil 4H-SiC samples was also characterized using  
249 200-kV TEM (JEOL, JEM-2000FX).

### 250 **3. Results**

#### 251 3.1 Microstructure in He<sup>+</sup>-ion-irradiated 4H-SiC

252 After irradiation, the internal microstructure of the He<sup>+</sup>-implanted 4H-SiC  
253 with a fluence of  $5 \times 10^{16} \text{ cm}^{-2}$  was examined, as shown in Fig. 1(a) together  
254 with the simulated damage and He<sup>+</sup> distribution profiles obtained using  
255 SRIM 2013. Because of the different irradiation damage levels, three types  
256 of regions with distinct bright-field image contrast (gray, black, and white)  
257 are discernible in Fig. 1(a), denoted as the A, B, and C layer, respectively,  
258 with the B layer further separated into B<sub>1</sub> and B<sub>2</sub> layers. As indicated by the  
259 TEM image contrast and selected-area diffraction, the near-surface layer (A  
260 layer) with gray contrast contained only minimal damage and still

261 maintained good crystallinity (as observed in Fig. 1(b)). However, in the  
 262 highest damage region, where the contrast was white (C layer), an  
 263 amorphous state was confirmed by observation of the diffraction, as shown  
 264 in Fig. 1(c). In addition, the two black layers (B<sub>1</sub> and B<sub>2</sub> layers) adjacent to  
 265 the amorphous layer appear to contain significant defects.



266  
 267 Fig. 1. Internal microstructure distribution of He<sup>+</sup>-irradiated 4H-SiC up to a fluence of 5  
 268 × 10<sup>16</sup> cm<sup>-2</sup>. (a) Cross-sectional micrograph of He<sup>+</sup>-implanted 4H-SiC and depth  
 269 distribution of displacement damage (white dashed line) and He concentration (red solid  
 270 line). (b, c) Diffraction patterns corresponding to the (b) A layer and (c) C layer. (d-f)  
 271 High-resolution TEM images obtained from different regions: (d) A layer, (e) B<sub>1</sub> layer,  
 272 and (f) near the interface between the B<sub>1</sub> and C layer. The images were taken near the  
 273 [11 $\bar{2}$ 0] zone axis.

274

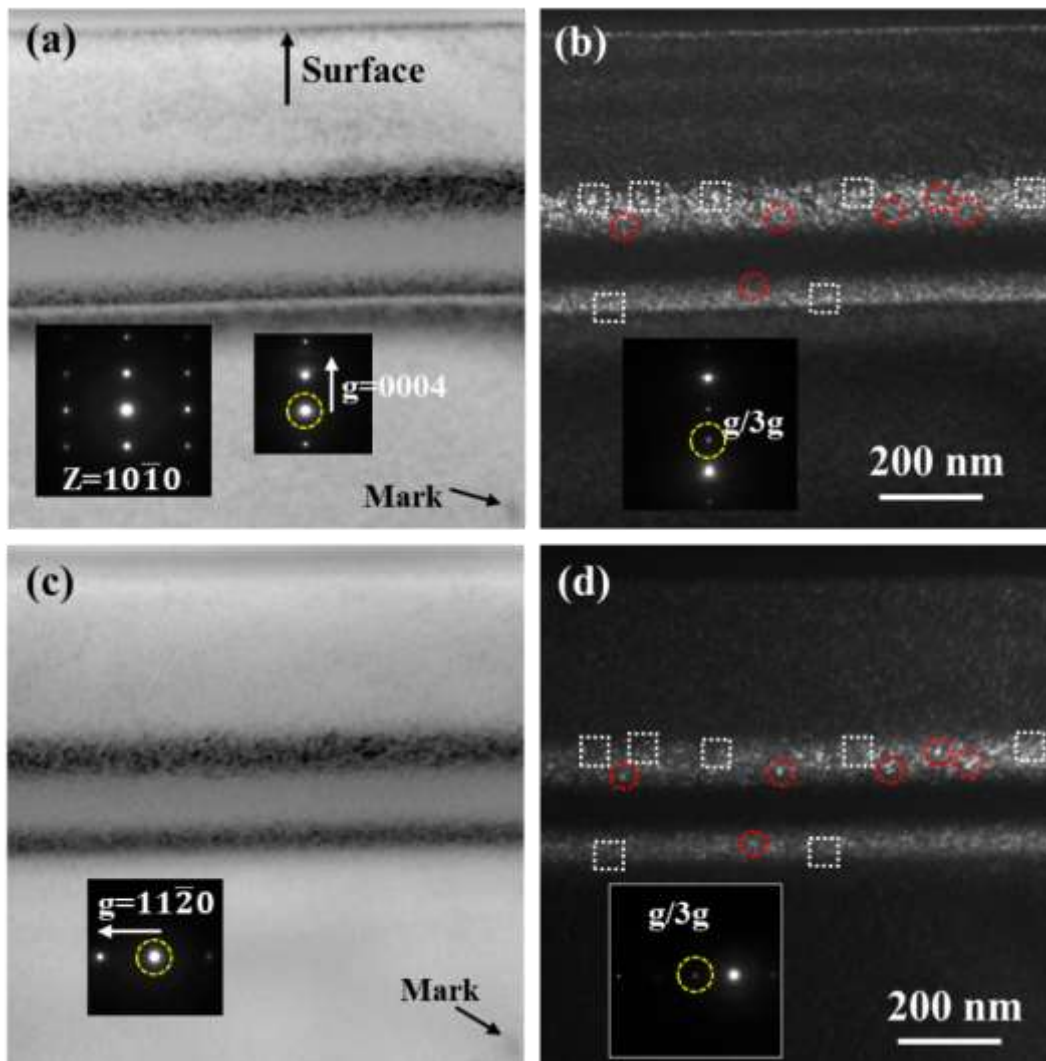
275 To resolve the defects in each region, HR-TEM images were obtained  
276 along the  $[11\bar{2}0]$  zone axis, which are displayed in Fig. 1(d-f), with Fig.  
277 1(d), 1(e), and 1(f) corresponding to the A layer, B<sub>1</sub> layer, and the interface  
278 between the B<sub>1</sub> and C layer (amorphous/crystal interface), respectively. In  
279 the A layer, the basal plane structure was maintained, which agrees well  
280 with the diffraction analysis shown in Fig. 1(b). In addition, the contrast of  
281 a few defects can be observed in Fig. 1(d). The main defects in the surface  
282 region might be point defects or tiny defect clusters that are difficult to  
283 clearly distinguish using HR-TEM [28]. However, in the relatively  
284 high-damage region (B<sub>1</sub> layers), the crystal exhibited obvious disorder (Fig.  
285 1(e)). Black spots are clearly observed in this image, which are so-called  
286 black spot defects (BSDs) [7,11,36], a type of point-defect clusters  
287 composed of vacancies and interstitials in irradiated SiC. A small fraction  
288 of these black spots may also correspond to small dislocation loops  
289 according to previously reported results [37]; however, here, we consider  
290 all of them to be BSDs for convenient discussion. Fig. 1(f) shows the  
291 microstructure near the amorphous/crystal interface; BSDs are also visible,  
292 and some even appear in the amorphous region like an island.

### 293 3.2 Defect distribution

294 The presence of lattice defects in crystalline materials leads the planes  
295 close to the defects to bend. Bending of the lattice planes results in a  
296 change of diffraction and therefore a change in the image contrast;  
297 information about the defects can thus be obtained by studying the contrast

298 in TEM [38]. To identify characteristics of the defect clusters (BSDs),  
299 different reflections corresponding to different sets of lattice planes were  
300 used to explore the defect distribution in selected-area He<sup>+</sup>-irradiated  
301 4H-SiC. The distributions of BSDs under different TEM two-beam  
302 observation conditions are presented in Fig. 2, with Fig. 2(a, b) obtained at  
303 diffraction vector  $g = [0004]$  and Fig. 2(c, d) obtained at  $g = [11\bar{2}0]$ . These  
304 images were obtained from the same area, and for orientation, a mark was  
305 made by focused-electron-beam irradiation using a JEM-2000FX (200 kV).  
306 Under the two-beam observation condition, the BSDs were clearly  
307 observed in both the bright-field and dark-field images as black spots (Fig.  
308 2(a) and 2(c)) and white spots (Fig. 2(b) and 2(d)), respectively. Comparing  
309 the images in Fig. 2(a) and (b) with those in Fig. 2(c) and (d), it is apparent  
310 that more BSDs appeared in the  $[0004]$  direction (Fig. 2(a) and (b)) than in  
311 the  $[11\bar{2}0]$  direction (Fig. 2(c) and (d)). Moreover, the defects observed  
312 with the reflection vector of  $[0004]$  became invisible with the reflection  
313 vector of  $[11\bar{2}0]$ , marked by a white square, and vice versa (marked by a  
314 red circle). The details of the lattice-plane bending generally depend on the  
315 characteristic of the defect [38]. According to the  $\mathbf{g} \cdot \mathbf{b} = 0$  invisible  
316 criterion for planar defects [39-41], the defects observed in Fig. 2 should be  
317 a type of planar defect that formed in the corresponding orientation or  
318 plane. Similar results were also observed for the reflection vectors  $g =$   
319  $[0004]$  and  $g = [10\bar{1}0]$  (Fig. S1 in supplementary material), with BSDs  
320 observed in one direction becoming invisible in the other direction. Hence,  
321 in these samples, the observed BSDs under different diffraction conditions

322 appeared to be the plane defects formed in each reflecting plane.



323

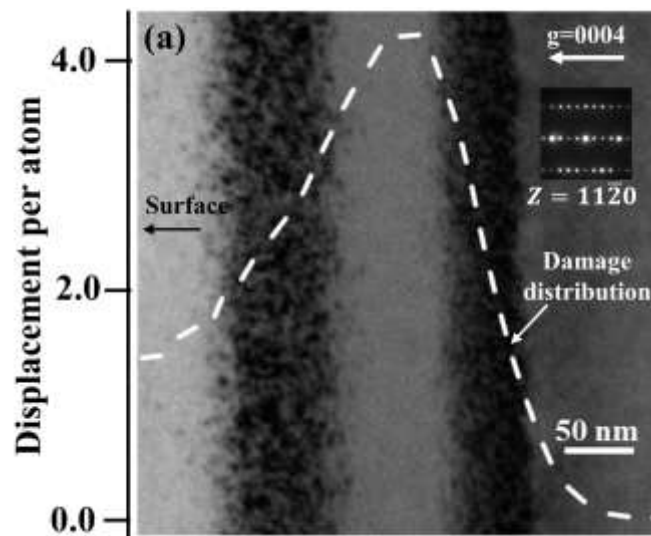
324 Fig. 2 TEM images of BSDs under different two-beam observation conditions: (a, b)  
325  $g=0004$  and (c, d)  $g=11\bar{2}0$ , with (a, c) bright-field images and (b, d) weak-beam  
326 dark-field images,  $g/3g$ . These images were obtained from the same area with a mark  
327 made for orientation purposes.

328

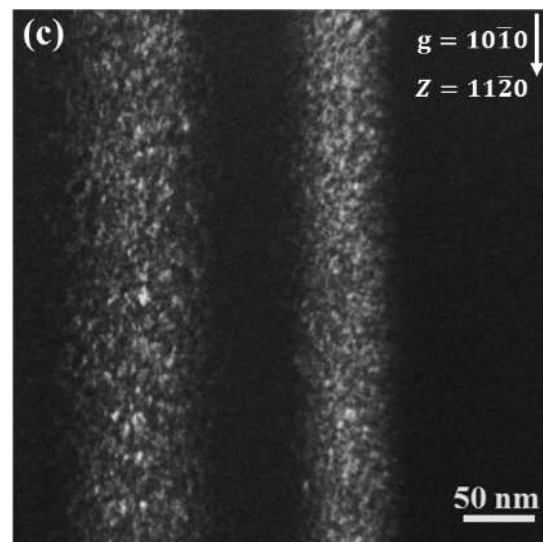
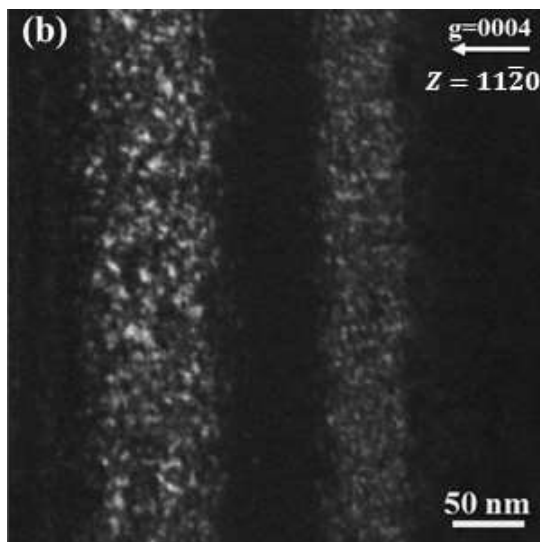
329 More detailed comparison of the defects formed in different orientations  
330 or planes was performed, as shown in Fig. 3. The images in Fig. 3(a)–(c)  
331 were obtained from the same area with Fig. 3(a) in the two-beam bright



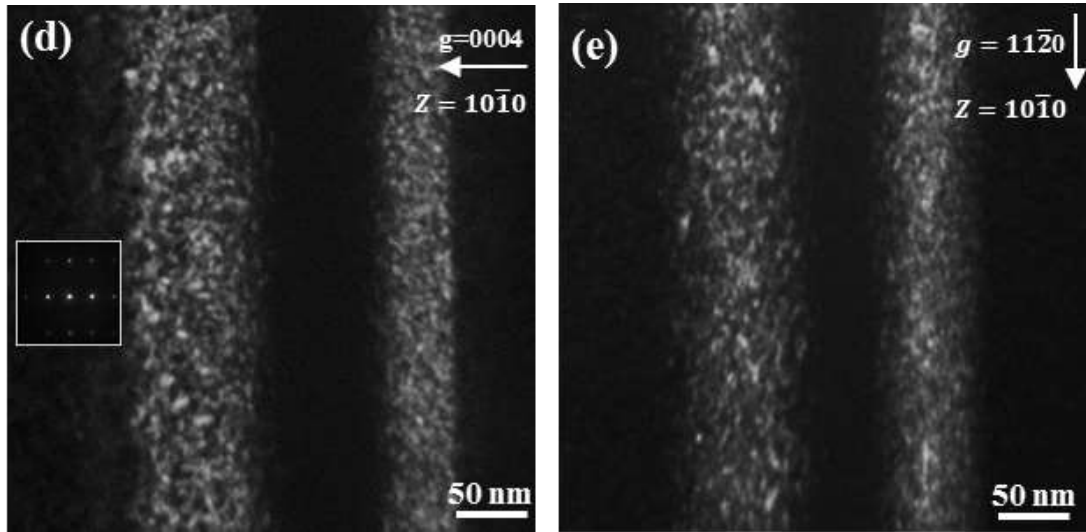
332 field condition (diffraction condition  $g=0004$ ) and Fig. 3(b) and 3(c) in  
 333 different weak-beam dark-field conditions ( $g/3g$ , with  $g=0004$  for (b) and  
 334  $g=10\bar{1}0$  for (c)). The images in Fig. 3(d) and 4(e) were also obtained from  
 335 the same area in different weak-beam dark-field conditions with  $g/3g$  and  
 336  $g=0004$  for Fig. 3(d) and  $g=11\bar{2}0$  for Fig. 3(e).



337



338



339

340 Fig. 3. TEM images of irradiated 4H-SiC taken under different observation conditions.  
 341 (a–c) were obtained from the same position: (a) two-beam bright-field image and (b, c)  
 342  $g/3g$  weak-beam dark-field images with  $g=0004$  for (b) and  $g=10\bar{1}0$  for (c). (d, e) were  
 343 obtained from same position with  $g/3g$  weak-beam dark field and  $g=0004$  for (d) and  
 344  $g=11\bar{2}0$  for (e).

345

346 These images show the different distributions of BSDs under different  
 347 diffraction conditions ( $g=0004$ ,  $g=10\bar{1}0$ , and  $g=11\bar{2}0$ ) in terms of the  
 348 defect size and number density. The average size and number density of  
 349 BSDs in region  $B_1$  with different diffraction conditions were counted using  
 350 weak-beam dark-field images, and the results are summarized in Table 1.  
 351 The BSDs appearing in the  $[0004]$  direction had the highest number density  
 352 followed by those in the  $[11\bar{2}0]$  and  $[10\bar{1}0]$  directions, and the average  
 353 size of BSDs formed in the  $[0004]$  direction was also substantially larger  
 354 than that in the  $[11\bar{2}0]$  and  $[10\bar{1}0]$  directions. In Fig. 4(a), the BSD size  
 355 distribution profiles for the  $[10\bar{1}0]$ ,  $[11\bar{2}0]$ , and  $[0004]$  directions greatly

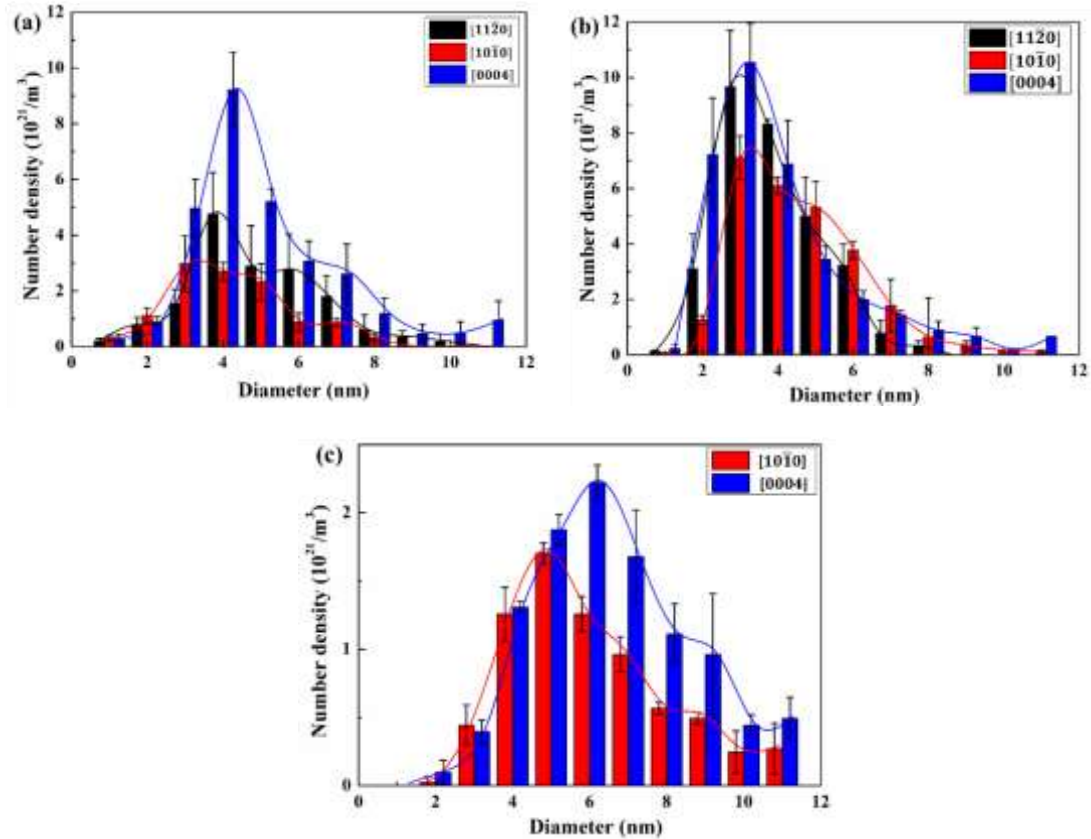
356 differ. Although the peak of the profile of the  $[10\bar{1}0]$ ,  $[11\bar{2}0]$ , and  $[0004]$   
 357 directions occurred at approximately 4 nm, the number density of relatively  
 358 large-size BSDs ( $\geq 8$  nm) was highest in the  $[0004]$  direction. In particular  
 359 for the  $[10\bar{1}0]$  profile, there was a lack of relatively large BSDs ( $\geq 8$  nm).  
 360 These results suggest an anisotropic defect distribution in the selected-area  
 361 ion-irradiated 4H-SiC, and the anisotropy of the BSD distribution can be  
 362 summarized as more and larger BSDs preferentially forming in the  $[0004]$   
 363 orientation compared with in the  $[10\bar{1}0]$  and  $[11\bar{2}0]$  orientations.  
 364 Table 1 Average size and number density of BSDs in different orientations.  
 365 The error bars represent the standard deviations

Conditions	$11\bar{2}0$	$10\bar{1}0$	0004	
Selected-area ion irradiation	Average size (nm)	4.5	3.9	5.5
		$\pm 0.78$	$\pm 0.52$	$\pm 0.33$
	Number density ( $10^{22} \text{ m}^{-3}$ )	1.6	1.1	2.9
		$\pm 0.15$	$\pm 0.18$	$\pm 0.28$
Non-selected-area ion irradiation	Average size (nm)	4.7	5.0	4.7
		$\pm 0.35$	$\pm 0.58$	$\pm 0.52$
	Number density ( $10^{22} \text{ m}^{-3}$ )	3.1	2.7	3.5
		$\pm 0.62$	$\pm 0.45$	$\pm 0.68$
Electron irradiation	Average size (nm)		6.2	7.1
			$\pm 0.39$	$\pm 0.17$
	Number density ( $10^{22} \text{ m}^{-3}$ )		0.72	1.1
			$\pm 0.018$	$\pm 0.015$

366

367

368



369

370

371 Fig. 4. Size distribution of BSDs in different orientations: (a) selected-area  
 372 ion-irradiated sample, (b) non-selected-area ion-irradiated sample, and (c)  
 373 electron-irradiated thin-film TEM sample. The error bars represent the standard  
 374 deviations.

375

### 376 3.3 Nature of defect type

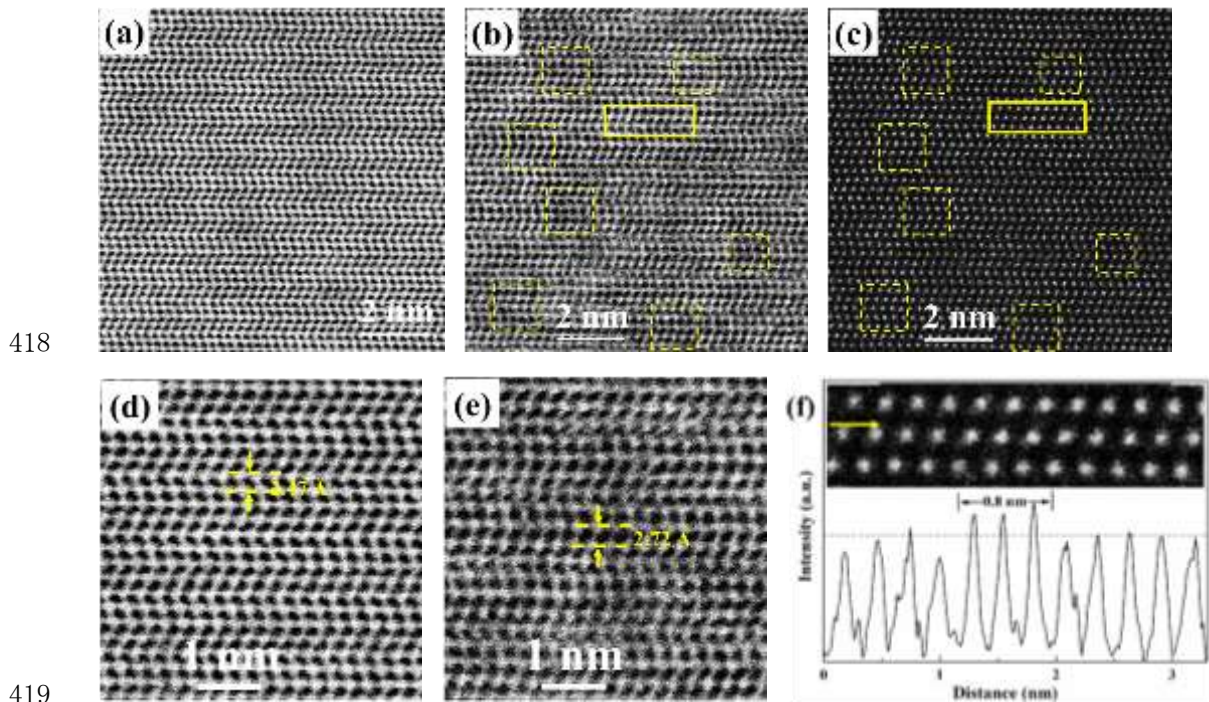
377 The nature of the irradiation-induced defect clusters was explored using  
 378 ABF-STEM and HAADF-STEM. HAADF-STEM is a robust technique for  
 379 identifying the position of atoms and atomic columns. When applied in a  
 380 restricted zone-axis orientation, the contrast in a HAADF image is strongly  
 381 dependent on the atomic number ( $Z^n$ , where  $n \approx 1.7$ ) and the local thickness  
 382 [42], which provides an approximate method for identifying atomic species.

383 ABF-STEM imaging can also be used to directly detect the position of  
384 atoms [43], providing a complementary contrast to HAADF, as shown in  
385 Fig. 5. For instance, the Si atom columns correspond to the black spots in  
386 the ABF-STEM images and the bright spots in the HAADF-STEM images.

387 The ABF- and HAADF-STEM images in Fig. 5(b) and (c) were  
388 obtained from the same region in the A layer (Fig. 1(a)), which was  
389 relatively less damaged. Compared with the STEM-ABF image obtained  
390 from the unirradiated area (Fig. 5(a)), the defect-induced contrast variation  
391 in the STEM image can be clearly observed even in this low-damage  
392 region, with some areas becoming relatively blacker and brighter in the  
393 ABF (Fig. 5(b)) and HAADF image (Fig. 5(c)), respectively. This can be  
394 attributed to the lattice disorder induced by the tiny defect clusters [44].  
395 The areas of tiny defect clusters are circumscribed by a dashed line, and the  
396 locations of these areas in the ABF and HAADF images agree well.

397 To clearly display the contrast variation, parts of the areas from Fig. 5(b)  
398 and (c) were enlarged and are presented in Fig. 5(e) and (f), respectively;  
399 the image in Fig. 5(d) (enlarging from Fig. 5(a)) is provided as a  
400 comparison standard. Using Gatan Digital Micrograph software, the  
401 measured average (0004) plane spacing from an inverse fast Fourier  
402 transform (IFFT) pattern in the unirradiated area is approximately 2.47 Å,  
403 as shown in Fig. 5(d), almost the same as the previously reported result of  
404 2.51 Å determined using XRD [45]. However, in the area with contrast  
405 change, the lattice plane spacing was increased to approximately 2.72 Å on  
406 average. The expansion of the lattice plane might be attributed to the tiny

407 interstitial-type cluster formed in these areas [46]. In addition, the area with  
 408 contrast variation in the HAADF image marked by a solid line in (Fig. 5(c))  
 409 was enlarged and is displayed in Fig. 5(f). The difference in image contrast  
 410 is corroborated by the intensity profiles displayed beneath the  
 411 corresponding columns, which were obtained using Gatan  
 412 DigitalMicrograph software across the column along the arrow direction.  
 413 The intensity of the center columns of this selected area increased. As there  
 414 was no heavier atom doped into the materials, the increased contrast might  
 415 arise from the interstitial-type clusters [(47),48)]. The ABF- and  
 416 HAADF-STEM results for the A layer suggest that most of the tiny defect  
 417 clusters observed in the A layer should be interstitial-type defects.



420 Fig. 5. STEM images obtained from unirradiated area and A layer along the  $[11\bar{2}0]$   
 421 zone axis. (a) ABF image from unirradiated area. (b) ABF image and (c) HAADF image  
 422 obtained from same region in the A layer. (d) Enlarged image of the area in (a). (e)

423 Enlarged image of the area in (b). (f) Enlarged image of the area marked by the solid  
424 line in (c) and the intensity of each atom column along the arrow direction. The  
425 contrast-changed areas are marked by dashed lines and solid lines.

426

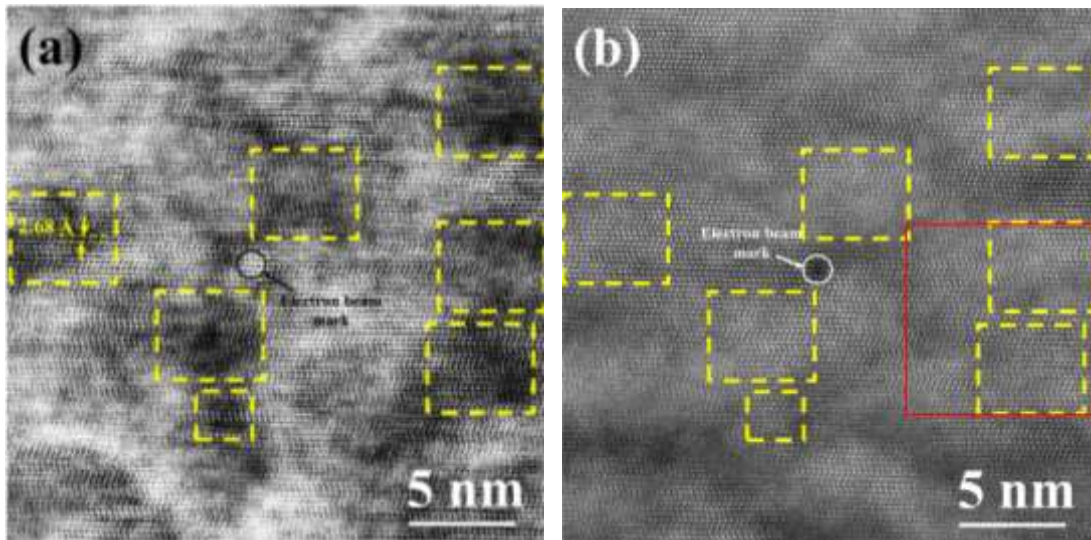
427 BSDs are usually identified in HR-TEM images by the black image  
428 contrast, as observed in Fig. 1(e). Comparing the ABF-STEM image and  
429 HR-TEM image in the same area (Fig. S2 in supplementary material), it is  
430 apparent that the BSDs also appeared as black contrast in the ABF-STEM  
431 image.

432 Using ABF- and HAADF-STEM, some larger contrast-changed areas  
433 circumscribed by dashed lines were observed in the B<sub>1</sub> layer and near the  
434 amorphous/crystal interface, as shown in Fig. 6. These contrast-changed  
435 areas can be attributed to the BSDs. In addition, the average size of these  
436 contrast-changed areas in Fig. 6 is approximately 5 nm, agreeing well with  
437 the size of BSDs summarized in Table 1, which also supports their  
438 designation as BSDs. The lattice-plane spacing was also expanded in these  
439 areas. Moreover, in some areas, such as in Fig. 6(c), which was enlarged  
440 from the area in Fig. 6(b) circumscribed by the red solid line, some extra  
441 planes of atom columns were observed, as confirmed by the IFFT image of  
442 this area (Fig. 6(d)). These extra planes also indicate that most defects  
443 formed in the contrast-changed areas should be interstitial type. Therefore,  
444 the above results suggest that the BSDs formed in our samples should  
445 mainly be interstitial-type clusters, which is consistent with the mobility of  
446 interstitials and vacancies in SiC. Bockstedte et al. reported that the

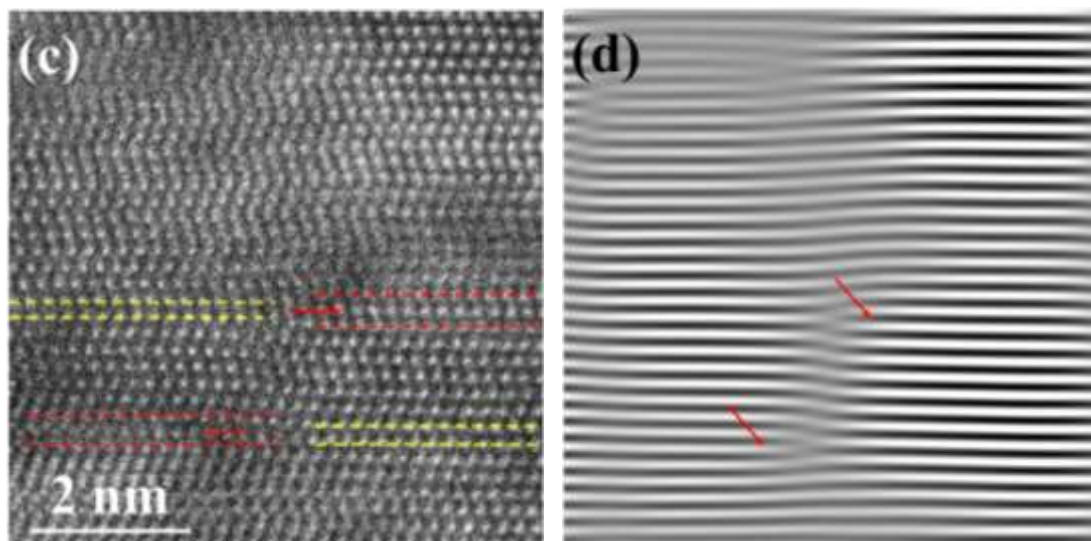
447 migration energies of vacancies are 3.2–3.6 eV and 3.5–5.2 eV in Si and C  
448 [49], respectively, whereas the migration energies of interstitials have been  
449 reported to be 1.53 eV in Si and 0.74 eV in C [50]. The Si vacancies in SiC  
450 become sufficiently mobile at 800 °C–900 °C [51], and C vacancies may  
451 require a higher temperature. It should be pointed out that interstitials are  
452 believed to be immobile based on the thermal equilibrium dynamics at  
453 room temperature. However, it has also been reported that during the  
454 ballistic collision process, the energy deposition from ions to a crystalline  
455 could also cause local heating (i.e., an elastic thermal spike) and intense  
456 ionization that can lead to localized electronic excitations and local lattice  
457 heating (i.e., an inelastic thermal spike). Besides, experimental results have  
458 demonstrated that this energy deposition could result in defect formation,  
459 diffusion and local structures driven far from equilibrium [52]. Recently, it  
460 has also found that the associated defects recovery and diffusion, due to the  
461 inelastic thermal spike and localized electronic excitation, are independent  
462 of ambient sample temperature [53]. Moreover, molecular dynamics  
463 simulation has confirmed the enhanced fission gas diffusion in UO<sub>2</sub> due to  
464 the ionization-induced thermal spike [54]. Therefore, the defect clusters  
465 (i.e., BSDs) formed in our samples might be attributed to the  
466 irradiation-enhanced defect diffusion. As interstitials have a lower  
467 migration energy barrier compared with vacancies, they could relatively  
468 easily move and combine into clusters in our study. In addition, M.  
469 Bockstedte et al. [55] investigated the annealing of vacancies and  
470 interstitials in SiC by an ab initio method based on density-functional



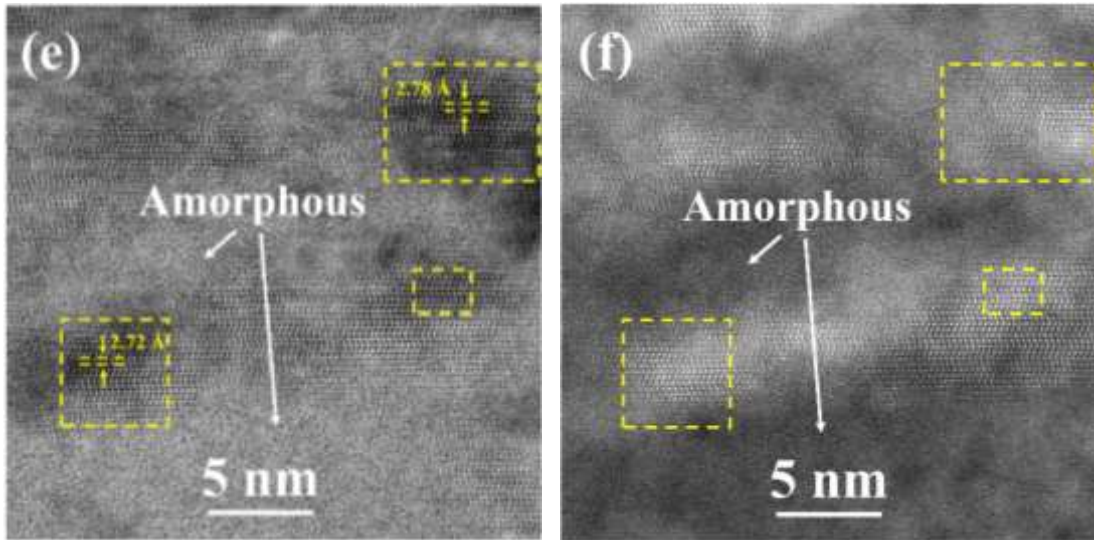
471 theory, which found that the higher mobility of carbon and silicon  
472 interstitials compared to the vacancies at lower temperatures drives the  
473 formation of interstitial carbon clusters. C. Liu et al. [7] developed a cluster  
474 dynamic model by regarding the BSD as an interstitial cluster and  
475 proposing additional physical phenomena likely to be present in irradiated  
476 SiC. The cluster distributions predicted by their simulations yield an  
477 agreement with those measured experimentally, which also supports that  
478 BSDs are interstitial type defects.



479



480



481

482 Fig. 6. STEM image obtained from B<sub>1</sub> layer and near the amorphous/crystal interface  
 483 along the  $[11\bar{2}0]$  zone axis. (a, b) were obtained from same region in the B<sub>1</sub> layer: (a)  
 484 ABF image and (b) HAADF image. (c) is enlarged from the area in (b) circumscribed  
 485 by the red solid line. (d) Image of inverse fast Fourier transform of (c). (e, f) were  
 486 obtained from the same region near the amorphous/crystal interface: (e) ABF image and  
 487 (f) HAADF image. In (a) and (b), a mark was made by an electron beam to confirm the  
 488 position of each image.

#### 489 **4. Discussion**

##### 490 **4.1 Anisotropic defect distribution**

491 The samples in the current study were selected-area ion irradiated such  
 492 that SiC could freely expand in the Z direction with swelling in the lateral  
 493 direction (X and Y directions) constrained. These conditions resulted in  
 494 anisotropic strain or swelling in the sample with a tensile strain in the Z  
 495 direction and compressive strain in the X and Y directions. The X, Y, and Z  
 496 directions correspond to lattice orientations of  $[11\bar{2}0]$ ,  $[10\bar{1}0]$ , and  $[0004]$   
 497 in these samples, respectively [32].

498 The anisotropic BSD distribution was determined using conventional  
499 TEM, and these defect clusters should mainly be interstitial type in view of  
500 the STEM results and defect mobility in SiC. As BSDs correspond to the  
501 accumulation of point defects, the formation of more and larger BSDs in  
502 the [0004] orientation implies that more interstitial defects were  
503 preferentially redistributed in the [0004] orientation compared with in the  
504 other two orientations. The defect distribution is correlated to the  
505 strain/swelling in the sample. In general, interstitial defects cause the  
506 expansion of the lattice around them. The detected defect distribution  
507 implies that the tensile strain introduced in the [0004] orientation should be  
508 higher than that in the other two orientations. This deduction agrees well  
509 with the anisotropic strain condition of our samples with tensile strain in  
510 the [0004] orientation and compressive strain in the  $[10\bar{1}0]$  and  $[11\bar{2}0]$   
511 orientation [32]. Moreover, even though with relative lower number density,  
512 the BSDs in the  $[10\bar{1}0]$  and  $[11\bar{2}0]$  direction are still expected to expand  
513 the lattice of the corresponding direction, compressive strain is introduced  
514 in these two directions. This implies that more defects with negative  
515 volume effect, i.e., vacancy [56] and/or carbon antisite defects (carbon  
516 atom occupying the Si-vacancy site,  $C_{Si}$ ) [4,27,57], than interstitial defects  
517 should be introduced in these two directions. It is well known that  
518 vacancies are simultaneously introduced into SiC with interstitials;  
519 however, the presence of  $C_{Si}$  defects remains unclear.

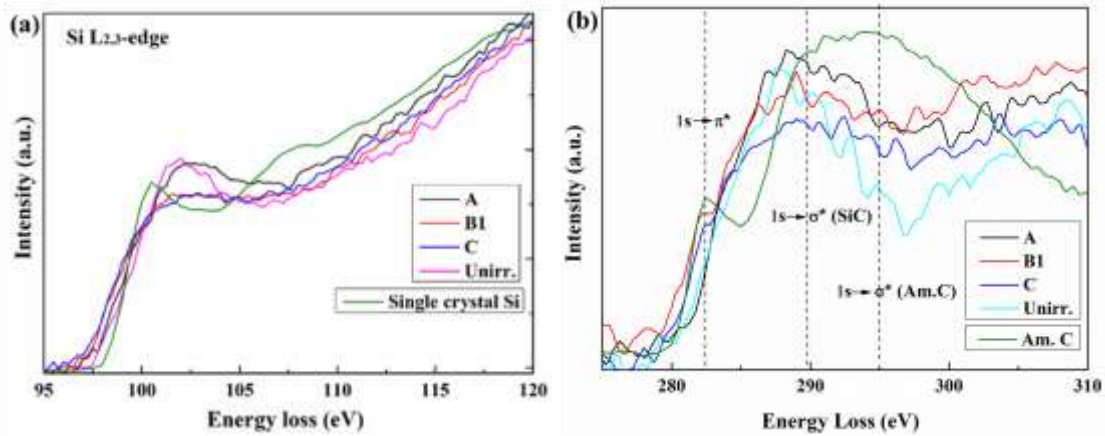
520 Fig. 7(a) and (b) display the STEM-EELS core-loss spectra of the  
521 silicon  $L_{2,3}$ -edge and carbon K-edge, respectively, acquired from different

522 damaged layers. To facilitate identification, the reference spectra of  
523 single-crystal silicon and amorphous carbon are also presented in Fig. 7(a)  
524 and 7(b), respectively. The core-loss of EELS spectrum could provide the  
525 insight into the bonding structure of materials with its peak position and  
526 peak shape. For the SiC crystal lattice structure, it is tetrahedral that the  
527 carbon atom is surrounded by four silicon atoms, corresponding to the  $sp^3$   
528 mode with the bond of C–Si, and this bonding structure shows the  $1s \rightarrow \sigma^*$   
529 peak at about 290 eV of the core-loss carbon K-edge spectrum, such as the  
530 spectrum of “Unirr” in the Fig. 7(b). For amorphous carbon, it shows the  
531 graphite like structure that carbon atom is surrounded by three carbon  
532 atoms, corresponding to a  $sp^2$  configuration, which shows both  $\pi^*$  (C=C)  
533 and  $\sigma^*$  (C–C) peaks at about 283 eV and 295 eV [58,59], respectively, such  
534 as the spectrum of “Am. C” in the Fig. 7(b). It is clear that the transition of  
535 C-Si bond to C–C and/or C=C bond in the SiC require a displacement of Si  
536 atom with C atom, which would result in the formation of  $C_{Si}$  (carbon atom  
537 occupying the Si-vacancy site), i.e., the appearance of peak at about 283 eV  
538 ( $1s \rightarrow \pi^*$ ) and 295 eV ( $1s \rightarrow \sigma^*$ ) in the carbon K-edge core-loss EELS  
539 spectrum would be evidence of the presence of  $C_{Si}$ .

540 For the core-loss EELS spectra in the  $He^+$  irradiated SiC, the peaks  
541 gradually broadened with increasing damage (from the A to C layer) in  
542 terms of the Si  $L_{2,3}$ -edge peak at  $\sim 103$  eV (Fig. 7(a)) and the carbon K-edge  
543  $1s \rightarrow \sigma^*$  peak at about 290 eV, especially for the B1 and C layer, which  
544 indicates the damage or decreasing of the C-Si tetrahedral bond structure in  
545 SiC. As comparing the “unirr” spectrum with the “A” spectrum in the Fig.

546 (b), it is shown that the left side (280~290 eV) of the  $\sigma^*$  peak (290 eV)  
547 seems not broadening. However, its right side (290~300 eV) becomes  
548 broadened and smoothing, and this energy region just corresponds to the  
549 carbon  $\sigma^*$  peak (295 eV) of the “Am. C” spectrum. This may suggest the  
550 appearance of carbon  $\sigma^*$  peak at 295 eV, and also the formation of C–C  
551 bond structure and the  $C_{Si}$ . With increasing damage, such as the B1 and C  
552 layer, the broadening of this peak (290 eV) at the region of 290~300 eV  
553 becomes more dominant. Moreover, a  $1s \rightarrow \pi^*$  shoulder peak (283 eV) was  
554 also observed in the spectra acquired from the B1 and C layer, which  
555 further confirms the presence of  $C_{Si}$  in the selected-area irradiated 4H-SiC.  
556 It should be pointed out that the formation of  $1s \rightarrow \pi^*$  peak (283 eV)  
557 indicates the irradiation-induced bonding configuration shifting from  $sp^3$  to  
558  $sp^2$  in SiC, which requires a highly damaged state, such as the formation of  
559 defect clusters or amorphization. Thus, it is observed only in the B1 and C  
560 layer. The transition of C–Si to C–C (and/or C=C) bond detected in our  
561 previous Raman analysis also implies the occurrence of the  $C_{Si}$  [32]. In  
562 previous works of Kondo et al. [4], an increase in the population of antisite  
563  $C_{Si}$  was also observed in  $Si^{2+}$ -irradiated SiC fiber, which was implicated as  
564 the primary cause for the shrinkage of the irradiated SiC fibers.  
565 Considering the negative volume effect of  $C_{Si}$  [4,60], the antisite defect of  
566  $C_{Si}$  may be dominantly located in  $([11\bar{2}0])$  and  $([10\bar{1}0])$ , contributing to  
567 the lateral (X- and Y-direction) compressive strain in selected-area  
568 ion-irradiated 4H-SiC. Therefore, in the selected-area ion-irradiated  
569 4H-SiC, it is likely that interstitial defects are preferentially redistributed in

570 the freely expanding direction (Z, [0004] orientation) with vacancy and/or  
 571 carbon antisite defects dominantly located in the constrained swelling  
 572 direction (X and Y, [11 $\bar{2}$ 0] and [10 $\bar{1}$ 0] orientation).



573

574 Fig. 7 Irradiation-induced change of EELS core-loss spectra: (a) Si L<sub>2,3</sub>-edge spectra  
 575 and (b) carbon K-edge spectra. The inset letters correspond to the layers marked in Fig.  
 576 1(a). Reference spectra of single-crystal silicon and amorphous carbon obtained from  
 577 the Gatan EELS website (<https://eels.info/atlas/carbon>) are provided for ease of  
 578 identification.

579

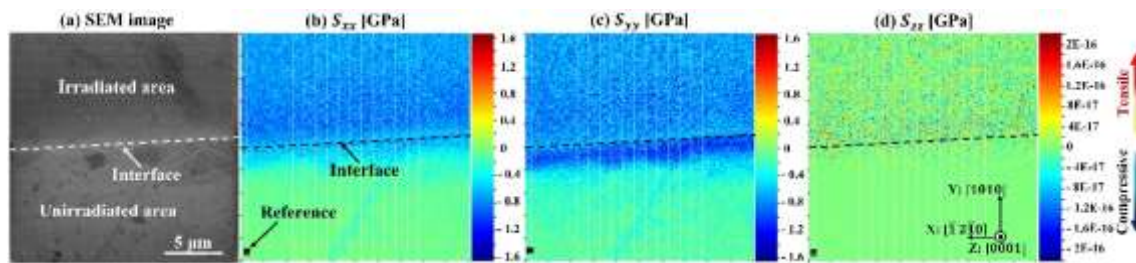
#### 580 4.2 Potential mechanism for anisotropic defect distribution

581 The different number density and size distribution of BSDs (shown in  
 582 Table 1 and Fig. 4(a)) indicate different nucleation and growth conditions  
 583 for the different orientations or planes. It is apparent that BSDs in the [0004]  
 584 orientation have more nucleation sites and a higher growth rate. Defect  
 585 formation and growth in SiC during ion irradiation mainly arise from the  
 586 irradiation-induced point defects and their diffusion and combination. Ion  
 587 irradiation usually introduces nearly the same number of interstitials and

588 vacancies (Frenkel pairs) in SiC. The anisotropic defect distribution in our  
589 sample can mainly be attributed to the different mobilities of interstitials  
590 and vacancies, which usually control the defect type and distribution. As  
591 the sample was irradiated at room temperature, where interstitial point  
592 defects are mobile and vacancies are not, it is likely that some of the  
593 interstitials might be redistributed from the  $[10\bar{1}0]$  and  $[11\bar{2}0]$   
594 orientations to the  $[0001]$  orientation to reduce the internal energy because  
595 of the habit plane for  $(0001)$ , resulting in larger and more interstitial-type  
596 BSDs in the interplane of  $[0004]$ .

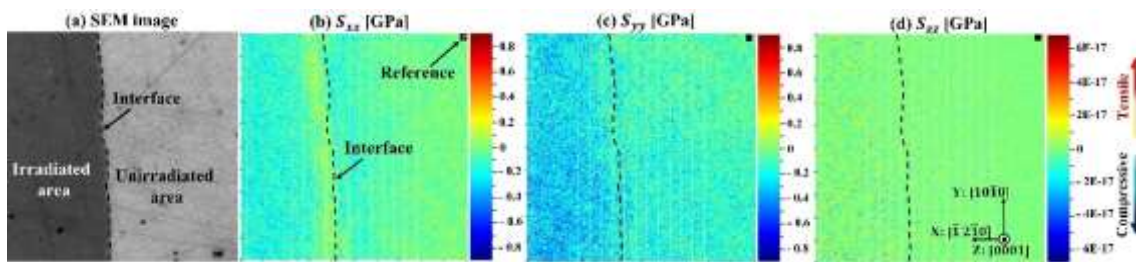
597 It has been reported that differential swelling leads to significant stresses  
598 [18,24]. Using EBSD, the stress distributions in irradiated and unirradiated  
599 areas were measured, as shown in Fig. 8 with (b), (c), and (d)  
600 corresponding to the stress in the X ( $[11\bar{2}0]$ ), Y ( $[10\bar{1}0]$ ), and Z ( $[0001]$ )  
601 directions, respectively. It is clear that because of the restriction of swelling,  
602 great compressive stress was introduced in both the X and Y directions with  
603 an average of  $-0.94$  and  $-1.15$  GPa, respectively; however, little stress  
604 arose in the Z direction because of the relaxation of swelling. Moreover, the  
605 stress distribution in the other sample with substantially lower fluence of  
606  $1 \times 10^{15} \text{ cm}^{-2}$  was also measured by EBSD, as shown in Fig. 9. The  
607 anisotropic stress distribution was also distinct in this sample with  
608 relatively large compressive stress in the X ( $-0.23$  GPa) and Y ( $-0.36$  GPa)  
609 directions but little in the Z direction. This result indicates that the  
610 compressive stress in the lateral direction begins to accumulate even at the  
611 beginning of irradiation. Kondo et al. [61] reported that compressive stress

612 likely inhibits the interstitial-type loop nucleation in planes perpendicular  
 613 to the stress axis, resulting in an anisotropic Frank loop development in  
 614 ion-irradiated SiC. In Table 1 and Fig. 4(a), the BSDs in the lateral  
 615 direction have a lower number density and smaller size. It is likely that the  
 616 lateral compressive stress introduced during irradiation inhibits the  
 617 nucleation and growth of interstitial defects. This anisotropy of the defect  
 618 distribution in selected-area He<sup>+</sup>-irradiated 4H-SiC can be mainly attributed  
 619 to the different stress conditions in the different directions.



620

621 Fig. 8. Stress distribution in selected-area He<sup>+</sup>-irradiated 4H-SiC with fluence of  $5 \times 10^{16}$   
 622  $\text{cm}^{-2}$ : (a) SEM image and (b)–(d) corresponding stress composition in (b) X, (c) Y, and  
 623 (d) Z direction. The strain distribution in this region is provided in the supplementary  
 624 materials of Ref. [32].



625

626 Fig. 9. Stress distribution in selected-area He<sup>+</sup> irradiated 4H-SiC with fluence of  $1 \times 10^{15}$   
 627  $\text{cm}^{-2}$ : (a) SEM image and (b)–(d) corresponding stress composition in (b) X, (c) Y, and  
 628 (d) Z direction.

629

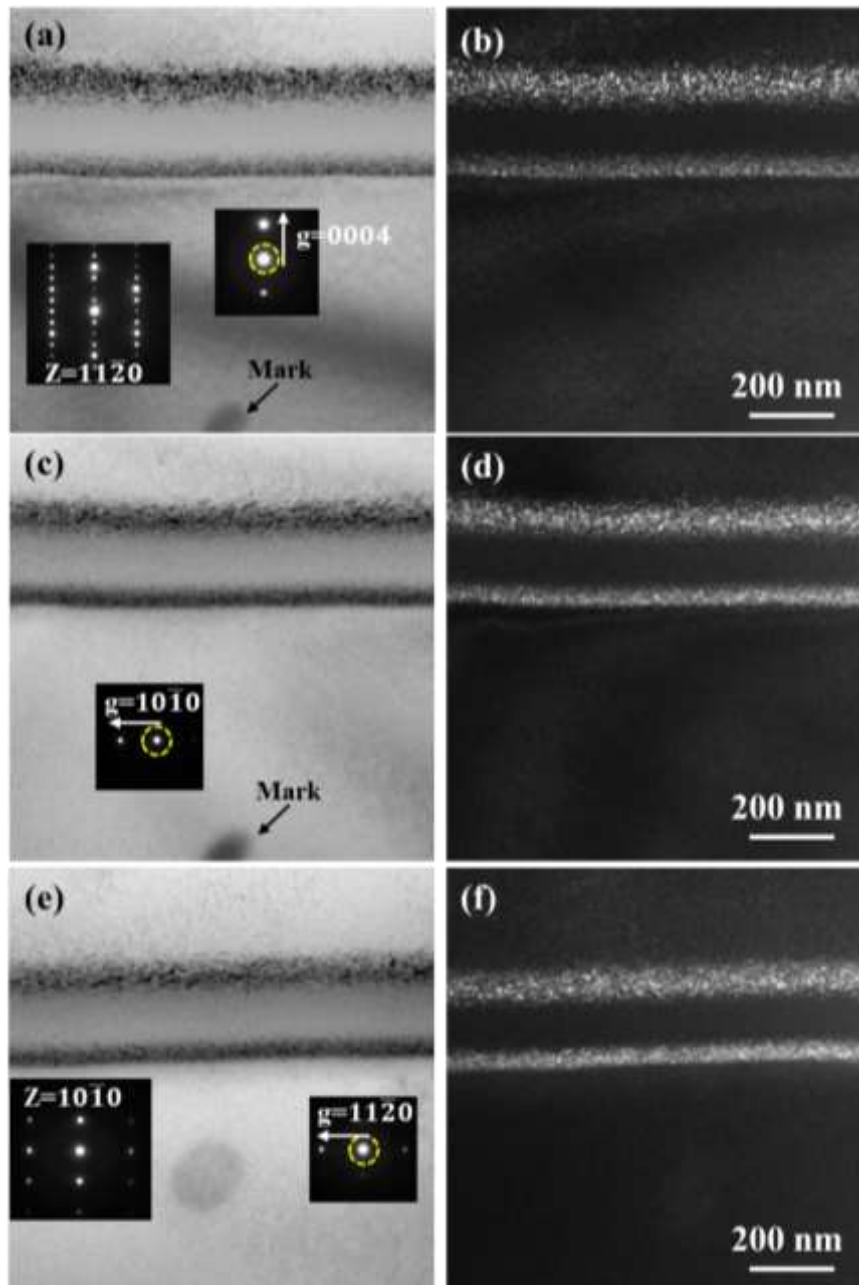


### 630 4.3 Defect distribution in non-selected-area He<sup>+</sup>-irradiated 4H-SiC

631 For comparison, a non-selected-area He<sup>+</sup>-irradiated 4H-SiC sample was  
632 prepared using the same fluence of  $5 \times 10^{16} \text{ cm}^{-2}$ . The defect distribution in  
633 this sample is shown in Fig. 10. The observed difference in the different  
634 directions in this sample appears to be smaller than that in the selected-area  
635 irradiated 4H-SiC (Fig. 2). The calculated average size and number density  
636 of the BSDs are summarized in Table 1. The BSDs in different directions  
637 were similar in average size with a higher number density in the [0004]  
638 direction. The defect distribution remained slightly anisotropic in this  
639 sample. However, its anisotropy was substantially smaller than that in the  
640 selected-area irradiated samples in terms of the average size and number  
641 density of BSDs. This result is supported by the similar defect size  
642 distributions in the different directions in Fig. 4(b). Without constraint in  
643 the lateral direction, the compressive stress introduced in the  
644 non-selected-area irradiated sample should be lower than that in the  
645 selected-area irradiated sample. The relatively lower anisotropy of the  
646 defect distribution in the non-selected-area He<sup>+</sup>-irradiated 4H-SiC indicates  
647 the restraining effects of the compressive stress on the formation of  
648 interstitial defects.

649 Although relatively smaller, an anisotropic defect distribution remained  
650 in this non-selected-area irradiated sample. It has been reported that  
651 compressive stress would also be introduced in the lateral direction in  
652 ion-irradiated SiC, which is attributed to the constraint against lateral  
653 expansion owing to the shallow thickness of the irradiated layer compared

654 with the sample thickness in contrast to the free expansion allowed along  
 655 the surface normal [61]. Hence, the anisotropic defect distribution in the  
 656 non-selected-area ion-irradiated sample may also be attributed to the  
 657 compressive stress introduced in the lateral direction.



658  
 659 Fig. 10 TEM images of BSDs in non-selected-area He<sup>+</sup>-irradiated 4H-SiC with fluence  
 660 of  $5 \times 10^{16} \text{ cm}^{-2}$ . (a), (c), and (e) are two-beam bright-field images with  $g=0004$ ,  $10\bar{1}0$ ,

661 and  $11\bar{2}0$ , respectively, and (b), (d) and (f) are their corresponding weak-beam  
662 dark-field images with  $g/3g$ . (a–d) were obtained from the same area, and (e, f) were  
663 obtained from another area.

664

#### 665 4.4 Defect distribution in electron-irradiated thin-film 4H-SiC

666 It has been reported that the introduction of compressive stress in the  
667 lateral direction may even be possible in non-selected-area ion-irradiated  
668 bulk samples because of the constraint against lateral expansion [61]. For  
669 comparison, the electron irradiation was performed on a TEM-foil sample  
670 of 4H-SiC at room temperature. Before irradiation, the samples were  
671 annealed at 600 °C for 30 min to remove any potential internal stress.  
672 During irradiation, the electron beam was parallel to the  $[11\bar{2}0]$  zone axis.  
673 Hence, compared with the  $\text{He}^+$ -irradiated bulk sample, there were two main  
674 differences in terms of the stress condition that should be noted in the  
675 electron-irradiated sample. One is that the lateral stress in the  
676 electron-irradiated area should be relatively lower because of the relatively  
677 thinner electron-irradiated sample, though electron irradiation is also a type  
678 of selected-area irradiation. The other is that the  $[0004]$  and  $[10\bar{1}0]$   
679 orientations should have a similar stress as both are lateral directions as the  
680 electron beam was along the  $[11\bar{2}0]$  direction. Therefore, the different  
681 stress states in the  $[0004]$  and  $[10\bar{1}0]$  orientations in the ion-irradiated  
682 sample could be neglected in this electron-irradiated sample.

683 The defect distributions in the centers of the electron-irradiated areas are  
684 shown in Fig. 11, and the counted average size and number density of

685 BSDs are summarized in Table 1. The size distribution of BSDs is shown in  
686 Fig. 4(c). The BSDs formed under electron irradiation were larger in  
687 average size and lower in number density than those under ion irradiation.  
688 This may be attributed to a larger flux density of electron beam irradiation  
689 ( $1.2 \times 10^{24} \text{ e} \cdot \text{m}^{-2} \cdot \text{s}^{-1}$ ) compared with the ion irradiation ( $6.2 \times 10^{16} \text{ He} \cdot \text{m}^{-2} \cdot \text{s}^{-1}$ )  
690 and also the surface effects of the TEM-foil sample. From the average size,  
691 number density, and size distribution of BSDs in the  $[10\bar{1}0]$  and  $[0004]$   
692 orientations, the defect distribution in electron-irradiated 4H-SiC also  
693 appears to be anisotropic. However, the ratios of the average size and  
694 number density between the  $[0004]$  and  $[10\bar{1}0]$  orientation were 1.15  
695 (7.1/6.2) and 1.52 (1.1/0.72) (Table 1), respectively, in the  
696 electron-irradiated sample, which are substantially smaller than the ratios  
697 of 1.41 (5.5/3.9) and 2.64 (2.9/1.1), respectively, in the selected-area  
698  $\text{He}^+$ -ion-irradiated sample. Therefore, it is apparent that the anisotropy of  
699 the defect distribution in the selected-area  $\text{He}^+$ -irradiated sample was  
700 enhanced, which can be primarily attributed to the compressive stress  
701 introduced in the lateral direction during irradiation.

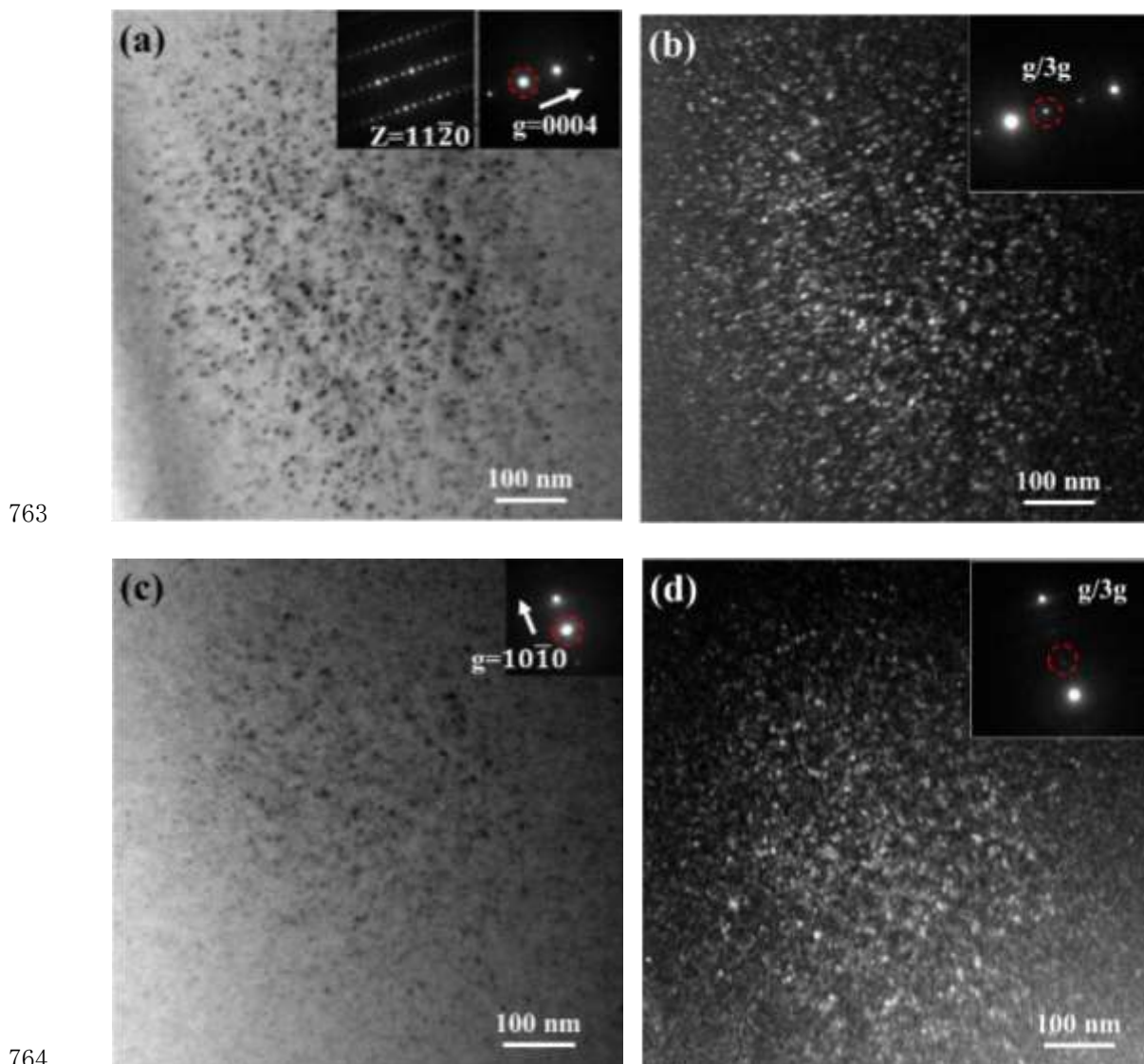
702 It should be noted that the different irradiation conditions for ion  
703 irradiation and electron irradiation, including the different dose rates,  
704 different irradiation particle energies, and the cascade effect, might  
705 contribute to the different defect evolution. In particular, interstitial and  
706 vacancy atoms might annihilate on the surface of the thin sample used in  
707 the electron irradiation, which would greatly affect the defect distribution  
708 in the sample. However, the above cases should have a similar effect on the

709 defect distribution for the [0004] and [10 $\bar{1}$ 0] directions, and they might not  
710 greatly change the anisotropy of the defect distribution between the [0004]  
711 and [10 $\bar{1}$ 0] directions. Hence, the great difference in the anisotropy of the  
712 defect distribution between the selected-area ion irradiation and electron  
713 irradiation can be mainly attributed to the compressive stress introduced  
714 during ion irradiation.

715         Similar to the non-selected-area He<sup>+</sup>-irradiated sample, anisotropic  
716 defect distribution was also somewhat introduced in the electron-irradiated  
717 foil sample. However, the stress effect on the anisotropy should be quite  
718 low in the electron-irradiated sample, as discussed above. Stress should not  
719 be the primary cause for the anisotropy between the [0004] and [10 $\bar{1}$ 0]  
720 directions in the electron-irradiated sample. Hence, the anisotropic defect  
721 distribution in the non-selected-area ion-irradiated sample and  
722 electron-irradiated sample might not only be attributed to the stress, and  
723 some other potential mechanisms might exist [27,31,62]. Anisotropic  
724 swelling is also observed in the reported result that a shrinkage of the a-axis  
725 is formed at extremely low doses of  $1.26 \times 10^{-3}$  dpa in H<sup>+</sup>-irradiated 6H-SiC  
726 with an expansion in the c-axis, which could be associated with  
727 irradiation-induced vacancies in the a-axis [27]. Therefore, the initial  
728 anisotropic distribution of defects in ion-irradiated  $\alpha$ -SiC might be  
729 attributed to the intrinsic property of  $\alpha$ -SiC, such as the larger parameter of  
730 the c-axis than that of a-axis. The interstitial atoms would expand the lattice,  
731 and the local crystal structure around a vacancy could contract. When a C  
732 or Si atom is removed from the lattice site in a unit cell of  $\alpha$ -SiC, a local

733 lattice strain is induced, and a repositioning of the surrounding atoms  
734 occurs to minimize the internal energy. The anisotropy of defect  
735 distribution, i.e., the interstitial atoms redistributed into c-axis (which is  
736 larger in plane space) and vacancies and/or  $C_{Si}$  located into the a-axis,  
737 seemly better to minimize the strain and disorder induced by irradiation.  
738 This interpretation agreed with the distribution of interstitial type defect of  
739 helium platelet, which has been reported to preferentially form in the c-axis  
740 [63]. In addition, the modeling results showed that the activation barrier for  
741 a migration of carbon interstitials in the 4H-SiC is the lowest along the  
742 c-axis ([0001]) compared with the  $[11\bar{2}0]$  and  $[10\bar{1}0]$  [64], which also  
743 agrees well with the defect distribution in our study. This suggests that the  
744 different migration energy for a defect along the different axes in the  $\alpha$ -SiC  
745 would also contribute to the anisotropic defect distribution and the  
746 anisotropic swelling. As the compressive stress is introduced into the a-axis,  
747 i.e., selected-area  $He^+$ -irradiated 4H-SiC, a higher anisotropic defect  
748 distribution is observed, which shows an enhanced tendency of defect  
749 repositioning discussed above. The compressive stress would compact the  
750 plane space in the a-axis, which seemly inhibits the interstitial type defect  
751 formation in this direction and enhances the anisotropic defect distribution  
752 in the  $He^+$  irradiated 4H-SiC. In addition, it has been reported that the  
753 irradiation-induced tensile strain would cause the drift of interstitial atoms,  
754 resulting in a higher tensile strain [65]. Considering the strain condition in  
755 the selected-area  $He^+$ -ion-irradiated 4H-SiC that tensile strain in the [0004]  
756 orientation and compressive strain in  $[10\bar{1}0]$  and  $[11\bar{2}0]$ , it is possible

757 that this strain condition would affect defect drift and enhance the  
758 anisotropic defect distribution, which would in turn result in higher  
759 anisotropic swelling. Therefore, the observed anisotropic defect distribution  
760 in the selected-area He<sup>+</sup>-irradiated 4H-SiC should be attributed to the  
761 integrated effects, including both the intrinsic properties of  $\alpha$ -SiC and the  
762 compressive stress in a-axis.



765 Fig. 11. TEM images of BSD distribution in the center of electron irradiation area of  
766 electron-irradiated 4H-SiC: (a, b)  $g=0004$  and (c, d)  $g=10\bar{1}0$ , with (a, c) bright-field

767 images and (b, d) weak-beam dark-field images,  $g/3g$ . These images were obtained from  
768 the same area.

769

## 770 **5. Summary**

771 Using TEM techniques, the defect distribution in selected-area  
772  $\text{He}^+$ -irradiated 4H-SiC with irradiation-induced anisotropic swelling was  
773 explored, and anisotropy of the defect distribution was observed. Interstitial  
774 defects were preferentially redistributed to the freely expanding direction  
775 (Z direction, [0004] orientation) with negative volume defects dominantly  
776 located in the constrained swelling directions (X and Y directions,  
777  $[11\bar{2}0]$  and  $[10\bar{1}0]$  orientations). This anisotropy of the defect  
778 distribution was substantially larger than that in non-selected-area  
779  $\text{He}^+$ -irradiated 4H-SiC and electron-irradiated thin-foil 4H-SiC.  
780 Compressive stress was introduced in the lateral direction (X and Y  
781 directions,  $[10\bar{1}0]$  and  $[11\bar{2}0]$  orientations), with little introduced in the  
782 surface normal direction (Z direction, [0004] orientation) in the  
783 selected-area  $\text{He}^+$ -irradiated 4H-SiC because of the constraint against  
784 lateral expansion, and these compressive stresses were introduced at the  
785 beginning of ion irradiation. The compressive stress introduced during  
786 irradiation was speculated to inhibit the formation of interstitial defects,  
787 enhancing the anisotropic defect distribution in the selected-area  
788 ion-irradiated 4H-SiC.

789



790 **Acknowledgements**

791 This work was partly supported by JSPS KAKENHI Grant Numbers  
792 JP19K22035 and JP19H00799. Part of this work was conducted at the  
793 Joint-Use Facilities at Hokkaido University, supported by the “Project for  
794 promoting public utilization of advanced research infrastructure (Program  
795 for supporting introduction of the new sharing system) grant number  
796 JPMXS0420100519” and the “Nanotechnology Platform” program of the  
797 Ministry of Education, Culture, Sports, Science and Technology (MEXT),  
798 Japan. The authors thank Mr. R. Ota for his help with the STEM  
799 experiments. Dr. Yang acknowledges stipend support from the Chinese  
800 Scholarship Council to perform this work at Hokkaido University. The  
801 authors would also like to thank Tiffany Jain, M.S., from Edanz Group  
802 (<https://en-author-services.edanzgroup.com/ac>) for editing a draft of this  
803 manuscript.

804

805 **References**

- 806 [1] Y. Zhang, R. Sachan, O. H. Pakarinen, M. F. Chisholm, P. Liu, H. Xue,  
807 W. J. Weber, Ionization-induced annealing of pre-existing defects in silicon  
808 carbide, Nat. Commun. 6, 8049 (2015).
- 809 [2] L. Nuckols, M. L. Crespillo, C. Xu, E. Zarkadoula, Y. Zhang, W. J.  
810 Weber, Coupled effects of electronic and nuclear energy deposition on  
811 damage accumulation in ion-irradiated SiC, Acta Mater. 199 (2020) 96–  
812 106.

- 813 [3] N. Daghbouj, B. S. Li, M. Callisti, H. S. Sen, J. Lin, X. Ou, M. Karlik,  
814 T. Polcar, The structural evolution of light-ion implanted 6H-SiC single  
815 crystal: Comparison of the effect of helium and hydrogen, *Acta Mater.* 188  
816 (2020) 609-622.
- 817 [4] S. Kondo, T. Hinoki, M. Nonaka, K. Ozawa, Irradiation-induced  
818 shrinkage of highly crystalline SiC fibers, *Acta Materialia* 83 (2015) 1–9.
- 819 [5] N. G. Wright, A. B. Horsfall, K. Vassilevski, Prospects for SiC  
820 electronics and sensors, *Mater. Today* 11 (2008).
- 821 [6] M. Li, X. Zhou, H. Yang, S. Du, Q. Huang, The critical issues of SiC  
822 materials for future nuclear systems, *Scr. Mater.* 143 (2018) 149–153.
- 823 [7] C. Liu, L. He, Y. Zhai, P. M. Voyles, K. Sridharan, D. Morgan, I.  
824 Szlufarska, Evolution of small defect clusters in ion irradiated 3C-SiC:  
825 Combined cluster dynamics modeling and experimental study, *Acta Mater.*  
826 125 (2019) 377–389.
- 827 [8] Yutai Katoh, Sosuke Kondo, Lance L. Snead, Microstructures of  
828 beta-silicon carbide after irradiation creep deformation at elevated  
829 temperatures, *J. Nucl. Materl.* 382 (2008) 170–175.
- 830 [9] G.S. Was, Z. Jiao, E. Getto, K. Sun, A.M. Monterrosa, S.A. Maloy, O.  
831 Anderoglu, B.H. Sencerc, M. Hackett, Emulation of reactor irradiation  
832 damage using ion beams, *Scrip. Mater.* 88 (2014) 33–36.
- 833 [10] Y. Katoh, L. L. Snead, I. Szlufarska, W. J. Weber, Radiation effects in  
834 SiC for nuclear structural applications, *Cur. Opin. Sol. State Mater. Sci.* 16  
835 (2012)143–152.

- 836 [11] N. Daghbouj, B.S. Li, M. Callisti, H.S. Sen, M. Karlik, T. Polcar,  
837 Microstructural evolution of helium-irradiated 6H-SiC subjected to  
838 different irradiation conditions and annealing temperatures: A multiple  
839 characterization study, *Acta Mater.* 181 (2019) 160–172.
- 840 [12] S. Leclerc, A. Declémy, M. F. Beaufort, C. Tromas, J. F. Barbot,  
841 Swelling of SiC under helium implantation, *J. Appl. Phys.* 98 (2005)  
842 113506.
- 843 [13] S. Leclerc, M.F. Beaufort, A. Declémy, J.F. Barbot, Evolution of  
844 defects upon annealing in He-implanted 4 H-SiC, *Appl. Phys. Lett.* 93  
845 (2008) 122101.
- 846 [14] A. Debelle, L. Thome, D. Dompont, A. Boulle, F. Garrido, J Jagielski,  
847 D. Chaussende, Characterization and modelling of the ion-irradiation  
848 induced disorder in 6H-SiC and 3C-SiC single crystals, *J. Phys. D: Appl.*  
849 *Phys.* 43 (2010) 455408.
- 850 [15] F.W. Clinard, Jr., W. Dienst, E.H. Farnum, Issues related to mechanical  
851 properties of neutron-irradiated ceramics, *J. Nucl. Materl.* 212-215 (1994)  
852 1075–1080.
- 853 [16] I.T. Yano T, Swelling and microstructure of AlN irradiated in a fast  
854 reactor, *J. Nucl. Materl.* 203 (1993) 249–254.
- 855 [17] T. Yano, M. Akiyoshi, K. Ichikawa, Y. Tachi, T. Iseki, Physical  
856 property change of heavily neutron-irradiated Si<sub>3</sub>N<sub>4</sub> and SiC by thermal  
857 annealing, *J. Nucl. Materl.* 289 (2001) 102.

- 858 [18] C.A.C. Silva, C. Shih, T. Koyanagi, Y. Katoh, S. J. Zinkle, Anisotropic  
859 swelling and microcracking of neutron irradiated Ti<sub>3</sub>AlC<sub>2</sub>–Ti<sub>5</sub>Al<sub>2</sub>C<sub>3</sub>  
860 materials, *Scr. Mater.* 114 (2016) 74–78.
- 861 [19] J.C. Nappé, C. Maurice, Ph. Grosseau, F. Audubert, L. Thomé, B.  
862 Guilhot, M. Beauvy, M. Benabdesselam, Microstructural changes induced  
863 by low energy heavy ion irradiation in titanium silicon carbide, *J. European*  
864 *Ceram. Soc.* 31 (2011) 1503–1511.
- 865 [20] Z. Li, R. C. Bradt, Thermal expansion of the hexagonal (4H) polytype  
866 of SiC, *J. Appl. Phys.* 60 (1986) 612.
- 867 [21] H. Kroncke, S. Figge, B.M. Epelbaum, D. Hommel, Determination of  
868 the temperature dependent thermal expansion coefficients of bulk AlN by  
869 HRXRD, *ACTA Phys. Polon. A*, 114 (2008) 1193-1200.
- 870 [22] T. H. Scabarozi, S. Amini, O. Leaffer, Thermal expansion of select  
871 phases measured by high temperature x-ray diffraction and dilatometry, *J.*  
872 *Appl. Phys.* 105 (2009) 013543.
- 873 [23] S. Kondo, T. Koyanagi, T. Hinoki, Irradiation creep of 3C–SiC and  
874 microstructural understanding of the underlying mechanisms, *J. Nucl.*  
875 *Materl.* 448 (2014) 487–496.
- 876 [24] S. Smolentsev, N.B. Morley, M. Abdou, Magnetohydrodynamic and  
877 thermal issues of the SiC<sub>f</sub>/SiC flow channel insert, *Fusion Sci. Technol.* 50  
878 (2006) 107–119.
- 879 [25] L.L. Snead, Y. Katoh, T. Koyanagi, K. Terrani, E.D. Specht,  
880 Dimensional isotropy of 6H and 3C SiC under neutron irradiation, *J. Nucl.*  
881 *Materl.* 471 (2016) 92–96.

- 882 [26] Y. Lin, C. Ho, W. Chuang, C. Ku, J. Kai, Swelling of ion-irradiated  
883 3C–SiC characterized by synchrotron radiation based XRD and TEM, J.  
884 Nucl. Materl. 455 (2014) 292–296.
- 885 [27] W. Jiang, P. Nachimuthu, W. J. Weber, L. Ginzburgsky, Variation in  
886 lattice parameters of 6H-SiC irradiated to extremely low doses, Appl. Phys.  
887 Lett. 91 (2007) 091918.
- 888 [28] Y. Zhang, W. J. Weber, W. Jiang, C. M. Wang, V. Shutthanandan, A.  
889 Hallen, Effects of implantation temperature on damage accumulation in  
890 Al-implanted 4H–SiC, J. Appl. Phys. 95 (2004) 4012.
- 891 [29] B. Tyburska-Püschel, Y. Zhai, L. He, C. Liu, A. Boule, P. M.  
892 Voyles, I. Szlufarska, K. Sridharan, Size distribution of black spot defects  
893 and their contribution to swelling in irradiated SiC, J. Nucl. Materl. 476  
894 (2016) 132–139.
- 895 [30] Y. Zhang, F. Gao, W. Jiang, D.E. McCready, W.J. Weber, Damage  
896 accumulation and defect relaxation in 4H-SiC, Phys. Rev. B 70 (2004)  
897 125203.
- 898 [31] S. Kondo, C. M. Parish, T. Koyanagi, Y. Katoh, Equilibrium shapes  
899 and surface selection of nanostructures in 6H-SiC, Appl. Phys. Lett. 110  
900 (2017) 142106.
- 901 [32] S. Yang, S. Tokunaga, M. Kondo, Y. Nakagawa, T. Shibayama,  
902 Non-destructive evaluation of the strain distribution in selected area He+  
903 ion irradiated 4H-SiC, Appl. Surf. Sci. 500 (2020).
- 904 [33] R. Devanathan, T. Diaz de la Rubia, W.J. Weber, Displacement  
905 threshold energies in b-SiC, J. Nucl. Materl. 253 (1998) 47–52.

- 906 [34] S. Yang, Y. Nakagawa, M. Kondo, T. Shibayama, electron energy-loss  
907 spectroscopic evaluation of depth-dependent swelling of He<sup>+</sup> ion-irradiated  
908 4H-SiC correlated with defect type, *J. Appl. Phys.* 127 (2020) 175106.
- 909 [35] K. Kamitani, M. Grimsditch, J.C Nipko, C.K. Loong, M. Okada, I.  
910 Kimura, The elastic constants of silicon carbide: A Brillouin-scattering  
911 study of 4H and 6H SiC single crystals, *J. Appl. Phys.* 82 (1997) 3152.
- 912 [36] B.S. Li, C. Zhang, H.P. Liu, L.J. Xu, X. Wang, Z. Yang, F.F. Ge, W.  
913 Gao, T.L. Shen, Microstructural and elemental evolution of polycrystalline  
914  $\alpha$ -SiC irradiated with ultra-high-fluence helium ions before and after  
915 annealing, *Fus. Eng. Des.* 154 (2020) 111511.
- 916 [37] Y. Katoh, N. Hashimoto, S. Kondo, L.L. Snead, A. Kohyama,  
917 Microstructural development in cubic silicon carbide during irradiation at  
918 elevated temperatures, *J. Nucl. Materl.* 351 (2006) 228–240.
- 919 [38] C.B. Carter, D.B. Williams, *Transmission electron microscopy: a text*  
920 *book for materials science*, Springer: New York, 1996.
- 921 [39] S. Sandlobes, M. Friak, S. Zaefferer, A. Dick, S. Yi, D. Letzig, Z. Pei,  
922 L.F. Zhu, J. Neugebauer, D. Raabe, The relation between ductility and  
923 stacking fault energies in Mg and Mg–Y alloys, *Acta Mater.* 60 (2012)  
924 3011–3021.
- 925 [40] H. Zhang, Zhongwen Yao, G. Morin, M. Griffiths, TEM  
926 characterization of in-reactor neutron irradiated CANDU spacer material  
927 Inconel X-750, *J. Nucl. Materl.* 451 (2014) 88–96.
- 928 [41] S. Sandlöbes, M. Friák, J. Neugebauer, D. Raabe, Basal and non-basal  
929 dislocation slip in Mg–Y, *Mater. Sci. Eng. A* 576 (2013) 61–68.

- 930 [42] Y. Lin, L. Chen, C. Hsieh, A. Hu, S. Lo, F. Chen, J. Kai, Atomic  
931 structure of nano voids in irradiated 3C-SiC, *J. Nucl. Materl.* 498 (2018)  
932 71–75.
- 933 [43] Eiji Okunishi, Hidetaka Sawada, Yukihiro Kondo, Experimental study  
934 of annular bright field (ABF) imaging using aberration-corrected scanning  
935 transmission electron microscopy (STEM), *Micron* 43 (2012) 538–544.
- 936 [44] J. Q. Liu, M. Skowronski, C. Hallin, R. Soderholm, H. Lendenmann,  
937 Structure of recombination-induced stacking faults in high-voltage SiC p- n  
938 junctions, *Appl. Phys. Lett.* 80 (2002) 749–751.
- 939 [45] A. L. Hannam, P. T. B. Shaffer, Revised X-ray Diffraction Line  
940 Intensities for Silicon Carbide Polytypes, *J. Appl. Cryst.* 2 (1969) 45.
- 941 [46] J. Li, Z. Wang, C. Chen, S. Huang, Atomic-scale observation of  
942 migration and coalescence of Au nanoclusters on YSZ surface by  
943 aberration-corrected STEM, *Sci. Rep.* 4 (2014) 5521.
- 944 [47] K. Watanabe, E. Asano, T. Yamazaki, Y. Kikuchi, I. Hashimoto,  
945 Symmetries in BF and HAADF STEM image calculations,  
946 *Ultramicroscopy* 102 (2004) 13–21.
- 947 [48] S. J. Pennycook, D. E. Jesson, High-resolution Z-contrast imaging of  
948 crystals, *Ultramicroscopy* 37 (1991) 14–38.
- 949 [49] M. Bockstedte, A. Mattausch, O. Pankratov, Ab initio study of the  
950 migration of intrinsic defects in 3C-SiC, *Phys. Rev. B* 68 (2003) 205201.
- 951 [50] F. Gao, W. J. Weber, Recovery of close Frenkel pairs produced by low  
952 energy recoils in SiC, *J. Appl. Phys.* 94 (2003) 4348–4356.

- 953 [51] E. Oliviero, M.F. Beaufort, J.F. Barbot, A. van Veen, A.V. Fedorov,  
954 Helium implantation defects in SiC: A thermal helium desorption  
955 spectrometry investigation, *J. Appl. Phys.* 93 (2003) 231–238.
- 956 [52] Y. W. Zhang, W. J. Weber, Ion irradiation and modification: The role of  
957 coupled electronic and nuclear energy dissipation and subsequent  
958 nonequilibrium processes in materials, *Appl. Phys. Rev.* 7 (2020) 041307.
- 959 [53] G. Veliša, E. Wendler, S. Zhao, et al. Delayed damage accumulation by  
960 athermal suppression of defect production in concentrated solid solution  
961 alloys, *Mater. Res. Lett.* 6 (2018) 136–141.
- 962 [54] M.W.D. Cooper, C.R. Stanek, J.A. et al. Simulation of radiation driven  
963 fission gas diffusion in UO<sub>2</sub>, ThO<sub>2</sub> and PuO<sub>2</sub>, *J. Nucl. Mater.* 481(2016)  
964 125.
- 965 [55] M. Bockstedte, A.r Mattausch, O. Pankratov, Ab initio study of the  
966 annealing of vacancies and interstitials in cubic SiC: Vacancy-interstitial  
967 recombination and aggregation of carbon interstitials, *Phys. Rev. B* 69  
968 (2004) 235202.
- 969 [56] P. H. Dederiches, C. Lehmann, H. R. Schober, A. Scholz, R. Zeller,  
970 lattice theory of point defects, *J. Nucl. Mater.* 69-70 (1978) 176-199.
- 971 [57] J. Li, L. Porter, S. Yip, Atomistic modeling of finite-temperature  
972 properties of crystalline b-SiC II. Thermal conductivity and effects of point  
973 defects, *J. Nucl. Materl.* 255 (1998) 139–152.
- 974 [58] L. Ponsonnet, C. Donnet, K. Varlot, J.M. Martin, A. Grill, V. Patel,  
975 EELS analysis of hydrogenated diamond-like carbon films, *Thin Solid*  
976 *Films*, 319 1998 97–100.



- 977 [59] S. Wakeland, R. Martinez, J. K. Grey, C. C. Luhrs, Production of  
978 graphene from graphite oxide using urea as expansion–reduction agent,  
979 Carbon, 48 (2010) 3463–3470.
- 980 [60] P.G. Baranov, I.V. Llyin, A.A. Soltamova, E.N. Mokhov, Identification  
981 of the carbon antisite in SiC: EPR of  $^{13}\text{C}$  enriched crystals, Phys. Rev. B 77  
982 (2008) 085120.
- 983 [61] S. Kondo, A. Kohyama, T. Hinoki, Anisotropic evolution of Frank  
984 loops in ion-irradiated silicon carbide, J. Nucl. Materl. 367-370 (2007)  
985 764–768.
- 986 [62] W. Jiang, W.J. Weber, Anisotropy of disorder accumulation and  
987 recovery in 6H–SiC irradiated with  $\text{Au}^{2+}$  ions at 140 K, J. Nucl. Materl. 389  
988 (2009) 332–335.
- 989 [63] R. W. Harrison, S.Ebert, J. A. Hinks, S.E. Donnelly, Damage  
990 microstructure evolution of helium ion irradiated SiC under fusion relevant  
991 temperatures, J. Eur. Ceram. Soc. 38 (2018) 3718-3726.
- 992 [64] E. Rauls, T.E.M. Staab, Z. Hajnal, Th. Frauenheim, Interstitial-based  
993 vacancy annealing in 4H–SiC, Physica B 308–310 (2001) 645–648.
- 994 [65] S. Leclerc, M.F. Beaufort, A. Declémy, J.F. Barbot, Strain-induced  
995 drift of interstitial atoms in SiC implanted with helium ions at elevated  
996 temperature, J. Nucl. Mater. 397 (2010) 132–134.